NASA
Technical
Paper
2018

June 1982

Laser Anemometer Measurements in an Annular Cascade of Core Turbine Vanes and Comparison With Theory

Louis J. Goldman and
Richard G. Seasholtz

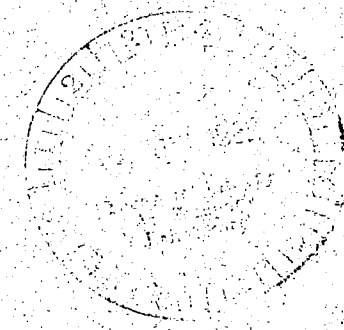

NASA

NASA
Technical
Paper
2018

1982

Laser Anemometer Measurements in an Annular Cascade of Core Turbine Vanes and Comparison With Theory

Louis J. Goldman and
Richard G. Seasholtz
Lewis Research Center
Cleveland, Ohio

NASA
National Aeronautics
and Space Administration

**Scientific and Technical
Information Branch**

Summary

A laser anemometer was employed to experimentally determine the velocity and flow angle in the blade-to-blade plane within and downstream of a core turbine stator vane cascade. The use of fluorescent seed particles to track the airflow allowed the laser measurements to be made to within 1 mm of the vane and endwall surfaces. The laser measurements were performed in an ambient-air inlet, full-annular cascade operating near the design, mean-radius, exit, critical velocity ratio of 0.78. Surveys of velocity and flow angle obtained at constant axial positions within the vane passage (every 10 percent) and at 1/2 axial chord downstream of the vanes are presented for constant radial positions near the hub, mean, and tip of the vanes. Measurements used to check for flow repeatability, flow periodicity, and incomplete-signal biasing errors are also included. A detailed description of the cascade inlet and vane geometry is presented, as well as formerly reported measurements of inlet boundary layer, vane surface static pressures, and downstream flow conditions and losses. The experimental laser measurements are presented in both plot and tabulated form so that they can be conveniently used as a test case for three-dimensional turbomachinery computer programs.

The experimental laser measurements generally agreed well with calculations from the inviscid, quasi-three-dimensional computer programs MERIDL and TSONIC, an indication of the usefulness of this analytic approach. The best agreement usually occurred at the mean radius and near the vane inlet. The largest differences of the measurements from theory were near the endwalls and toward the vane exit, where viscous and secondary flow effects and measurement uncertainty would be expected to be the greatest. For all the measurements within the vane passage (except at 1 percent of axial chord and 2.5 and 97.5 percent of span), the average difference and standard deviation of the measurements from theory were calculated to be 1.3 ± 3.0 percent in velocity and $2.1° \pm 1.5°$ in flow angle.

A particle dynamics calculation for 1.2-μm-diameter particles (the probable size of seed particles detected in this investigation) indicated that the seeding particles would generally track the airflow to within 2 percent in velocity and 1° in flow angle for most of the passage. However, differences of 2.5 to 4 percent in velocity and 2° to 3° in flow angle were calculated near the vane suction surface toward the vane inlet.

The experimental laser measurements were found to be repeatable and periodic within the accuracy of measuring the seed particle vector velocity, which was statistically estimated to be about 0.8 percent in velocity and 1.2° in flow angle. Because of the relatively low turbulence levels within the vane passage, incomplete-signal biasing errors were not observed in this investigation.

Introduction

The aerodynamic and heat transfer characteristics of advanced high-temperature core turbine vanes and blades are currently being experimentally investigated at the NASA Lewis Research Center. Highlights of this comprehensive research program have been reported in reference 1. As part of this effort the aerodynamic evaluation of the core turbine of reference 1 has been obtained from studies conducted in two-dimensional and full-annular cascades and from overall stage tests. None of these tests, however, included the details of the internal flow conditions within the turbine vane or blade passages. Knowledge of the internal flow conditions is very important to turbine designers and computational fluid dynamicists. Several papers dealing with internal flow measurements by laser anemometry have been presented in reference 2, but because details of the turbomachinery geometry are generally lacking, independent analytical comparisons are difficult.

This report presents the results of laser anemometer measurements taken within and downstream of a core turbine vane passage described in reference 1. Experimental measurements are compared with existing NASA turbomachinery computer program calculations (refs. 3 and 4) in order to check the applicability of these programs. Details of the cascade vane geometry and the inlet and exit flow conditions are included herein so that the experimental results can be used as a test case for other three-dimensional turbomachinery computer programs.

For the investigation reported herein a 508-mm-diameter, ambient-air inlet, full-annular cascade operating near the design, mean-radius, exit, critical velocity ratio of 0.78 was employed. Optical access of the laser beams was limited to the radial direction for this cascade, and therefore only velocity components in the blade-to-blade plane could be obtained by the fringe type of laser anemometer system. Radial components of velocity, however, are expected to be small for the axial-flow turbine stator vanes tested.

This report includes a detailed description of the full-annular cascade and laser anemometer, the experimental procedures used, and the results obtained. Surveys of velocity and flow angle obtained at constant axial positions within the vane passage (every 10 percent) and at 1/2 axial chord downstream of the stator vanes are presented for constant radial positions near the hub, mean, and tip of the vanes. Other survey results that were used to check for measurement repeatability, flow periodicity, and incomplete-signal biasing errors (similar to those described in ref. 5) are also included for completeness. Nondimensional laser measurements are presented herein in both plot and tabulated form. In addition, previously obtained measurements of inlet boundary layer (ref. 6), vane surface static pressures, and downstream flow conditions and losses (ref. 7) are included. Comparison of the experimental results with calculations from the inviscid, quasi-three-dimensional computer programs MERIDL and TSONIC (refs. 3 and 4) are also made and discussed.

Apparatus

Cascade Facility

The core turbine stator, full-annular cascade consisted primarily of an inlet section, a test section, and an exit section. The facility and a cross-sectional view of the facility are shown in figures 1 and 2, respectively. In operation, atmospheric air was drawn through the inlet section, the blading, and the exit section and then exhausted through the laboratory altitude exhaust system.

Inlet section. – The inlet, consisting of a bellmouth and a short straight section, was designed to accelerate the flow to uniform axial-flow conditions at the vane inlet. The bellmouth profile and coordinates are presented in figure 3.

Test section. – The test section, for this investigation, consisted of a sector of four vanes that were part of the full-annular ring of 36 vanes. The annular ring and the test section are shown in figure 4. A cutout in the test-section outer vane ring provided access for the laser beams. The test vanes in this region were machined to the vane tip radius in order to permit a window to fit flush with the tip endwall. The window is described in appendix B. (Symbols are defined in appendix A.)

The stator vane geometry is shown in figure 5. The untwisted vanes, of constant profile from hub to tip, had a height of 38.10 mm and an axial chord of 38.23 mm. The stacking axis of the vane was located at the center of the trailing-edge circle. The vane aspect ratio and the solidity at the mean radius (based on axial chord) were 1.0 and 0.93, respectively. The stator hub-tip radius ratio was 0.85 and the tip diameter was 508 mm. Additional geometric information is shown in figure 5. Turbine design information is presented in reference 8.

Exit section. – The exit section consisted of a dump-diffusing section and a flow-straightening section. The flow straightener was designed to turn the swirling flow back to the axial direction before it entered the laboratory altitude exhaust system. The straightener consists of a bundle of short tubes with centerlines parallel to the cascade axis.

Laser Anemometer

The argon-ion laser anemometer used for this study was a conventional fringe type of system similar to other anemometers used at the Lewis Research Center (refs. 5 and 9 to 11). The laser and optics (fig. 6) were mounted on a rigid plate that was moved by a traversing mechanism to survey the test region. The seed material was a fluorescent dye aerosol used to improve the signal-to-noise ratio when making measurements near the vanes and the endwalls. A microcomputer was used to control the traversing mechanism and for data handling (fig. 7). A complete description of the laser anemometer, including the theory, optics, traversing mechanism, windows, seeding, and electronics, is presented in appendix B.

Test Procedure

Cascade Flow Conditions

To operate the cascade facility, ambient air from the test cell was drawn through the cascade and exhausted into the laboratory altitude exhaust system. The test conditions in the cascade were set by controlling the pressure ratio across the vane row with two throttle valves located in the exhaust system. A hub static tap located downstream of the test section, where the flow was assumed to be nearly circumferentially uniform (station M, fig. 2), was used to set this pressure ratio. For this investigation the hub-static to inlet-total pressure ratio $p_{h,M}/p_0'$ was maintained at a value of 0.65. This corresponds to a mean-radius, ideal, exit, critical velocity ratio $(V_M/V_{cr})_{id,m}$ near the design value of 0.78. At this condition the design equivalent mass flow $W\sqrt{\theta_{cr}}/\delta$ through the cascade is 4.828 kg/sec.

Laser Anemometer Survey Measurements

The locations of the laser survey measurements are summarized in figure 8. Surveys were made at 11 axial planes (every 10 percent of axial chord) within the vane passage and at one plane approximately 1/2 axial chord downstream of the vane trailing edge. At a given axial plane, laser measurements were taken for one or more fixed radial positions at 1/3° increments across the

passage (fig. 8). Measurements were obtained at about 600 distinct points in the flow field.

At the vane mean radius, measurements were obtained at all 12 axial survey planes. Near the hub and tip (i.e., radial positions of 10 and 90 percent of span) measurements were made at eight axial planes (fig. 8). Measurements 1 millimeter from the endwalls (radial positions of 2.5 and 97.5 percent span) were obtained only at 20 and 80 percent of axial chord.

At any fixed point in the flow field, two components of velocity were measured so that the velocity magnitude and flow direction could be calculated. These velocity components were generally oriented ±20° from the expected flow direction in order to minimize incomplete-signal biasing errors that can occur in turbulent flows (ref. 5) and to allow measurements close to the vane surfaces. Because of the vane geometry, measurements close to the pressure surface could only have been made by tilting the laser beams from the radial direction. This would have required repositioning the laser probe volume after tilting the beams. The expenditure of time needed to do this was considered too large for the few extra data points that could have been obtained near the pressure surface. Therefore beam tilting was not used for this investigation. To obtain measurements near the suction surface, beam tilting was not necessary. However, measurements close to the suction surface were more difficult to obtain near the vane trailing-edge region. This was probably due to the centrifuging of the larger seed particles toward the pressure surface and the inability of the laser system to detect particles smaller than about 1 μm in diameter (i.e., the only particles remaining near the suction surface).

Calculation Procedure

Experimental Calculations

Velocity and turbulence. – At each measurement point, data were generally obtained at two fringe pattern orientations (φ_1 and φ_2) that gave velocity components (V_1 and V_2) at approximately ±20° from the expected flow direction α (see the section Test Procedure). The velocity components V_j lie in the blade-to-blade plane (as explained in appendix B), and the nomenclature and orientation are shown in figure 9. The velocity components V_j are calculated from the measured transit time and fringe spacing (eq. (B1)) and are related to the velocity magnitude V and flow angle α by

$$V_j = V\cos(\alpha-\varphi_j) \qquad j=1,2 \tag{1}$$

The velocity magnitude V and flow angle α are calculated from the two measured velocity components V_1 and V_2 by using equation (1) and are given by

$$\alpha = \arctan\left(\frac{V_1\cos\varphi_2 - V_2\cos\varphi_1}{V_2\sin\varphi_1 - V_1\sin\varphi_2}\right) \tag{2}$$

$$V = \frac{V_1}{\cos(\alpha-\varphi_1)} = \frac{V_2}{\cos(\alpha-\varphi_2)} \tag{3}$$

The velocity components V_j are actually the average or mean value of 1000 individual measurements. In addition to the mean value the standard deviation σ_j of the 1000 individual measurements is calculated. For isotropic turbulence, and in the absence of noise, the standard deviation σ_j is related to the turbulence intensity I_j of the flow by

$$I_j = \frac{\sigma_j}{V} \qquad j=1,2 \tag{4}$$

Incomplete-signal biasing errors. – In turbulent flows, incomplete-signal biasing errors can be caused by fluctuations in the flow direction, as has been fully described in reference 5 (where this bias is called angle biasing). This type of biasing occurs because the rate of the velocity component measurements, or data rate, depends on the flow angle: The data rate is larger for fluctuations that are more normal to the fringes. The analysis in reference 5 showed that the incomplete-signal biasing error was dependent on the turbulence intensity I_j (no biasing for zero turbulence), the number of fringes N, the particle size distribution, and the fringe pattern orientation φ_j (error increases as φ_j increases).

To check for incomplete-signal biasing errors in this investigation, the following procedure was used: At selected points in the flow field, velocity components V_j were measured over a wide range of fringe pattern orientations φ_j on either side of the expected flow direction α. In the absence of biasing errors, the velocity components V_j were related to the velocity magnitude V and the flow angle α by equation (1) for all values of φ_j. Therefore the measured components V_j were curve fit to equation (1) by using the method of least squares. The least-squares procedure for nonlinear functions, such as equation (1), is described in reference 12. The least-squares method results in the determination of the most probable value of the velocity magnitude V and the flow angle α for the set of measurements (as well as an estimate of the uncertainty in these values). The biasing error at a given fringe orientation φ_j is defined as

$$\text{Biasing error} = \frac{V_j - \hat{V}\cos(\hat{\alpha}-\varphi_j)}{\hat{V}\cos(\hat{\alpha}-\varphi_j)} \qquad j=1,2,\ldots,n \tag{5}$$

where n is the number of fringe orientations measured. If biasing errors occur in the measurement of the velocity components V_j, equation (1) will not represent the data

very well. Both the difference of the measurements from the least-squares curve fit values and therefore the biasing errors (eq. (5)) will be large.

Accuracy of measurements. – The accuracy, or uncertainty, of the measurements reported herein is based on a confidence interval of 95 percent (2σ value). The uncertainty in a given parameter was determined, when possible, by statistical means. That is, multiple-measurements of the parameter were made from which the standard deviation could be determined. For calculated parameters such as velocity magnitude V and flow angle α, the uncertainty was calculated by the method of reference 13. The uncertainties for the measurement parameters are summarized in table I. Two values are listed in table I for axial position Z as the result of a change in measurement technique. A depth micrometer was used for Z values up to 80 percent of axial chord; when this technique was no longer possible, a "linear" potentiometer was used.

Theoretical Calculations

Theoretical calculations were performed to determine the velocity of the air flowing through the vane passage and to determine how well the entrained seed particles tracked this airflow.

Air velocity. – The velocity of the air flowing through the vane passage was calculated by using the inviscid two-dimensional computer programs MERIDL and TSONIC described in references 3 and 4, respectively. The MERIDL program provides a solution on the hub-to-tip midchannel stream surface that is then used by the TSONIC program to obtain a solution on a number of blade-to-blade stream surfaces from hub to tip. A quasi-three-dimensional solution is obtained by requiring that, for each of the TSONIC solutions, the pressure- and suction-surface static pressures be equal near the vane trailing edge. This condition is obtained by slightly changing the downstream whirl distribution for the MERIDL program, redoing the TSONIC solutions, and iterating until the preceding static-pressure equality is satisfied to some tolerance limit. This procedure has been fully described in reference 14 and requires the user to make the downstream whirl distribution changes. This procedure was followed for the theoretical results reported herein.

Seed particle velocity. – The laser anemometer system measures the velocity of small seed particles entrained in the airflow, and therefore the ultimate measurement accuracy depends on how well the particles follow or track the flow. A particle dynamics calculation was made for this vane geometry to determine how well different sized particles track the airflow. These calculations were performed for a mean-radius, blade-to-blade stream surface by the method described in reference 15. For these calculations the seed particles are assumed to be spherical, of known uniform size, and moving through a known airflow field (results from MERIDL and TSONIC programs used herein). The seed particle trajectories were calculated with the assumption that the frictional or drag force on the particles follows Stokes' law. The difference between the calculated particle velocity and the airflow velocity, at a given point, is an estimate of how well these particles (of assumed size) will track the flow.

Results and Discussion

Laser Anemometer Measurements and Comparison with Theory

The laser survey measurements are presented in figures 10 to 21 for constant axial planes within the passage and for one axial plane downstream of the vanes. When measurements were made at more than one radial position (e.g., fig. 11), the results are presented by offsetting the critical velocity ratio V/V_{cr} axis as shown in these figures. The circumferential position θ axis is not offset. The tabulated values, presented in table II, contain, in addition to the calculated velocity magnitude V and flow angle α, the individual component measurements V_j. The experimental test conditions and measured vane surface circumferential locations are summarized in table III. The experimental measurements are compared with the theoretical results obtained from a quasi-three-dimensional inviscid calculation procedure by using the computer programs MERIDL (ref. 3) and TSONIC (ref. 4) as discussed in the section Calculation Procedure. These comparisons are discussed here for the following representative regions: (1) axial planes near the vane leading edge, (2) axial planes near midchord, (3) axial planes near the vane trailing edge, (4) an axial plane downstream of the vanes, and (5) blade-to-blade planes near the vane hub, mean, and tip.

Axial planes near vane leading edge. – The laser measurements obtained near the passage leading edge (i.e., at approximately 1, 10, 20, and 30 percent of axial chord are shown in figs. 10 to 13). Very close to the leading edge (fig. 10, approx 1 percent of axial chord) there is a large variation in flow angle from the suction side of the passage to the pressure side caused by flow around the vane circular leading edge. The measured flow angles exhibit this large flow angle variation but are generally (excluding the first two points near the suction surface) 0° to 6° higher than the theoretical results. The velocities are generally 3 to 6 percent lower than theory at this axial position. Considering the difficulty of both the measurement and calculation techniques near the leading edge, this comparison is thought to be reasonable. Downstream of the vane leading edge (figs. 11 to 13) there are smaller variations in the flow angle but larger variations in velocity from the suction side of the passage

to the pressure side. In general, the experimental data appear to be very smooth, except close to the hub and tip endwalls (fig. 12), and this may have been caused by light reflection or higher turbulence levels near these surfaces. The agreement between the measurements and theory for these axial positions (10 to 30 percent) are considered to be very good. The average difference and the standard deviation of the measurements from the theoretical results were calculated to be 0.6 ± 2.7 percent in velocity and $1.3° \pm 1.1°$ in flow angle (excluding the data at 2.3 and 97.4 percent of span). The largest differences in velocity occurred very close to the tip endwall (97.4 percent of span), where the measurements were 4 to 6 percent lower than theory. The largest flow angle differences occurred near the tip endwall (90 percent of span), where the measurements were 1° to 3° lower than theory.

Also shown in these figures are the calculated free-stream velocities near the vane surface that were obtained from vane surface tap pressure measurements. These data points agree well with the theoretical results and the trends in the experimental data. The data point shown in figure 12 by a "*X*" symbol was obtained from measurements used to check for biasing errors and is discussed later in this report.

Axial planes near midchord. – The laser measurements obtained near midchord (40, 50, and 60 percent of axial chord) are shown in figures 14 to 16. Both the experimental and theoretical flow angle results exhibit a minimum value between the suction and pressure sides of the passage. There appears to be more scatter in the flow angle measurements than there was near the vane leading edge. This was probably due to the higher turbulence levels that occurred in the flow in this region. This is discussed later. The theoretical variation of the critical velocity ratio across the passage was the largest for this region and was well followed by the laser measurements. The agreement between the measurements and theory for the midchord region was considered to be good. The average difference and standard deviation of the measurments from the theoretical results were calculated to be 2.5 ± 2.0 percent in velocity and $2.8° \pm 1.4°$ in flow angle. The largest differences occurred near the tip endwall (90 percent of span), where the measurements were lower than theory by 3 to 5 percent in velocity and 2° to 5° in flow angle.

Axial planes near vane trailing edge. – The laser measurements near the vane trailing edge (70, 80, 90, and 100 percent of axial chord) are shown in figures 17 to 20. For this region of the passage the theoretical variations from suction to pressure side tended to be smaller, and a number of unusual features (i.e., inflection points and minimums) are noted in the theoretical results. These unusual features were felt to be caused by the application of inviscid flow calculations to a region of high curvature at the vane trailing edge. This resulted in the calculation of velocities that were unrealistically high around the trailing edge, which in turn affected to some extent the flow-field calculations upstream. These unusual features do not appear in the experimental data. The data scatter was similar to that in the midchord region and also probably due to the higher turbulence levels in this region. The agreement between the measurements and theory for this region is considered reasonable. The average difference and standard deviation of the measurements from the theoretical results were calculated to be 0.7 ± 3.7 percent in velocity and $2.2° \pm 1.4°$ in flow angle (excluding the data at 2.3 and 97.3 percent of span). Of these measurements the largest differences in velocity occurred near the hub endwall (10 percent of span), where the measurements were between 3 percent lower and 8 percent higher than theory. Very close to the endwalls (fig. 18, 2.3 and 97.3 percent of span) the comparison between the measurements and theory was the poorest. This may be due to viscous and secondary flow effects in this region which are not accounted for in the theoretical results. The measurement uncertainty was also probably highest in these regions.

Axial plane downstream of vanes. – The laser measurements obtained approximately 1/2 axial chord downstream of the vanes are shown in figure 21. Survey results at 80 percent of span are shown in this figure since the laser beam damaged the plastic window at 90 percent of span (appendix B). The theoretical results are shown only to give an indication of the free-stream conditions and would not be expected to be valid in the wake regions, where viscous effects predominated. The downstream measurements are for flows from passages adjacent to the test passage because of constraints on the laser survey table circumferential motion and the large flowturning through the vanes. The multiple wake survey results, shown in figure 21, indicate that the flow was periodic.

The measured free-stream velocity levels for surveys at radial positions of 10, 50, and 80 percent of span agreed quite well with the theoretical results. The average difference and standard deviation of the measurements from the theoretical results were calculated to be -0.4 ± 0.9 percent in velocity. The measured free-stream flow angles were generally lower than theory but agreed quite well at 50 percent of span. The calculated average difference at 50 percent of span was $0.6° \pm 0.8°$. The agreements at the other radial positions were not nearly as good. The average difference and standard deviation of the measured flow angle in the free stream from the theoretical results were calculated to be $2.7° \pm 0.7°$ at 10 percent of span and $5.8° \pm 0.9°$ at 80 percent of span. On the whole, the comparison of the measurements and theory for the downstream location is considered to be

reasonable. Of course, this comparison excludes the wake regions, where a viscous calculation would be required.

Blade-to-blade planes near the vane hub, mean, and tip. – In the preceding sections measurements and theory were compared at constant axial planes. In this section similar comparisons (using the same experimental results) are discussed on constant blade-to-blade planes within the passage. In general the agreement of the measurements obtained near the hub, mean, and tip of the vanes (10, 50, and 90 percent of span, figs. 10 to 20) with theory was best at 50 percent of span. The average difference and standard deviation of the measurements from the theoretical results, for all axial positions within the vane passage (except at 1 percent axial chord) were calculated to be 2.0 ± 2.3 percent in velocity and $1.9° \pm 1.4°$ in flow angle for 50 percent of span. Corresponding values at the other radial positions were -1.0 ± 3.4 percent in velocity and $1.8° \pm 1.3°$ in flow angle at 10 percent of span, and 1.8 ± 3.1 percent in velocity and $2.8° \pm 1.5°$ in flow angle at 90 percent of span. For measurements very close to the endwalls (2.5 and 97.5 percent of span) the agreement with theory was generally poorer than at 90 percent of span and may have been due to viscous and secondary flow effects near these surfaces. The measurement uncertainty was also probably highest in these regions.

For all the measurements within the vane passage (except at 1 percent of axial chord and 2.5 and 97.5 percent of span), the average difference and standard deviation of the measurements from theory were calculated to be 1.3 ± 3.0 percent in velocity and $2.1° \pm 1.5°$ in flow angle. This agreement is considered reasonable.

Turbulence Measurements

The turbulence intensity at each individual measurement point is presented in table II. The overall features are shown in figure 22, where the circumferentially averaged turbulence intensity is presented as a function of axial position for a radial position of 50 percent of span. Also shown are the standard deviations, or spread, from these average values. The average turbulence intensity exhibited a minimum value of around 2.5 percent at 20 percent of axial chord and was fairly constant at about 3.5 percent from 50 percent of axial chord to the downstream measurement location. The spread in the average turbulence intensity was also smaller at 20 percent of axial chord than in the midchord or downstream regions. The turbulence intensity at the other radial survey positions exhibited similar behavior, although the values very close to the endwalls (2.5 and 97.5 percent of span) were generally higher (table II).

The turbulence intensity results (fig. 22) show quantitatively what was also observed qualitatively during the experimental investigations. That is, visual monitoring of the quality of the laser Doppler burst signals indicated that the flow appeared to be steadier near the vane leading-edge region (i.e., at 10, 20, and 30 percent of axial chord) than from the midchord to the downstream region. In addition, measurements made alternately at axial positions of both low and high turbulence levels (i.e., 20 and 80 percent of axial chord) on the same days indicated that these turbulence differences were not related to changes in system operation (seeding quality or humidity level).

Flow Repeatability, Periodicity, and Incomplete-Signal Biasing Errors

A number of additional data runs were performed during the investigation to insure data accuracy. These included checks of flow repeatability, flow periodicity, and incomplete-signal biasing errors (ref. 5). These experimental results are also included in table II (i.e., runs 7, 9, 11, 16, 20, 21, 25, 31, 32, 41, and 42) for completeness.

Flow repeatability. – To check for flow repeatability, a number of additional runs were made at previously surveyed locations throughout the vane passage (i.e., runs 7, 9, 11, 16, 20, 25, 31, and 32 in table II). Because these additional measurements were performed on different days, they are therefore not only a check on the repeatability of the laser measurement system but also a check on how well the cascade flow conditions and probe volume position could be duplicated. A typical flow repeatability comparison is shown in figure 23 for 20 percent of axial chord. The velocity and flow angle were generally found to be repeatable within the accuracy of the measurements.

Flow periodicity. – The measurements made downstream of the vanes, over three vane wakes, are one check of the flow periodicity (fig. 21). These results which have been discussed previously, indicated that the flow was periodic. An additional check was performed at 50 percent of axial chord by taking measurements in the passage adjacent to the test passage (run 21). These results are shown in figure 24, where the adjacent passage circumferential positions θ have been shifted one vane spacing (10°) for ease of comparison. These results also indicate that the flow is periodic.

Incomplete-signal biasing. – To check if incomplete-signal biasing errors, discussed in the section Calculation Procedure (refs. 5 and 9), could occur for measurements obtained within the passage, two additional runs were made (runs 41 and 42). For fixed points (R, θ) at 20 and 50 percent of axial chord, velocity components V_j were measured over a wide range of fringe pattern orientations φ_j on either side of the expected flow angle α. As explained in the section Calculation Procedure, the velocity component measurements were fit to equation

(1) by the method of least squares. The biasing errors were defined as the difference of the measured velocity component from that calculated from the least-squares fit. These results are shown in figure 25, where it can be seen that the biasing errors for both axial positions are small. Therefore incomplete-signal biasing errors did not occur within the passage. This result was not surprising, since previous measurements (ref. 9) indicated that incomplete-signal biasing errors occurred in high-turbulence-intensity I_j regions (i.e., in wake regions, where I_j was 7.5 percent) but did not occur in low-turbulence-intensity regions (i.e., in the free stream, where I_j was 2.5 percent). Since the turbulence intensity within the passage was generally less than 5 percent, incomplete-signal biasing errors would not be expected.

Another reason for doing these additional measurements over a wide range of fringe pattern orientations was to obtain a more accurate determination of the velocity magnitude V and the flow angle α. The increased accuracy, however, was obtained at a large expenditure of time required to make the multicomponent velocity measurements. These parameters, V and α, and an estimate of their accuracy were obtained from the least-squares curve fit procedure. The least-squares values of velocity magnitude V and flow angle α for these two axial positions (corresponding to runs 41 and 42) are shown, by the "X" symbol, in figures 12 and 15. These results agreed reasonably well with the other measurements. However, their estimated accuracy was determined to be 1/2 percent in velocity and 1/2° in flow angle (as compared with 0.8 percent in velocity and 1.2° in flow angle for the other measurements, table I).

Seed Particle Dynamics

A particle dynamics calculation was performed for this vane geometry to determine how well the seed material tracked the airflow. The method has been described in the section Calculation Procedure. The calculations were performed for 1.2-μm-diameter particles, which is the most probable size of the seed particles detected in this investigation (appendix B, the section Seeding). The results are shown in figure 26 as contour plots of the differences in velocity magnitude and flow angle between the seed particles and the gas flow (airflow) at the mean radius. Generally the flow angle differences were less than 1° and the velocity magnitude differences were less than 2 percent. However, close to the vane suction surface near the vane leading edge, the differences increased to around 2° to 3° and 2.5 to 4 percent. These results depend strongly on the seed particle size assumed for the calculation. For example, if the particle diameter were 1.4 μm (instead of 1.2 μm), the differences near the suction surface at the inlet would increase to about 4° to 6° and 3.5 to 6 percent.

Inlet, Vane Surface, and Exit Measurements

Previous reported measurements of the inlet boundary layer, vane surface static pressures, and downstream flow conditions and losses are included herein. The purpose is to allow the laser measurements to be more conveniently used as a test case for three-dimensional turbomachinery computer programs. These results are briefly discussed.

Inlet boundary layer measurements. – Boundary layer measurements of total pressure were made approximately 1 axial chord upstream of the vane leading edge (station 1, fig. 2) and were reported in reference 6. The boundary layer probe had an inside diameter of 0.2 mm. Wall static pressures were also measured at this location. The calculated boundary layer velocity profiles are presented in table IV and figure 27. The curves in the figure represent the least-squares curve fit of the data to the power-law profile

$$\frac{V}{V_{fs}} = \left(\frac{y}{\delta_{bl}}\right)^m \tag{6}$$

The dimensionless boundary layer thicknesses δ_{bl}/h determined by the least-squares procedures were 1.9 and 7.1 percent for the hub and tip walls, respectively. Similarly the values of m obtained were 0.158 and 0.076 for the hub and tip walls, respectively. For these values of m the resulting dimensionless displacement and momentum thicknesses (based on vane height h) were 0.255 and 0.193 percent for the hub and 0.502 and 0.436 percent for the tip, respectively.

Vane surface static pressure measurements. – Static pressures were measured on the vane surface near the hub, mean, and tip and were reported in reference 7. The static taps were 0.51 mm in diameter and normal to the vane surface. The measured pressures are presented in table V. The free-stream critical velocity ratios calculated from these pressures, shown in figure 28, compare well with the theoretical results calculated from the MERIDL and TSONIC computer programs. These static pressure results were also used previously in figures 11 to 19 of this report.

Vane exit measurements. – Survey measurements of flow angle, static pressure, and total pressure approximately 1/3 axial chord downstream of the vane were reported in reference 7. The combination probe employed tubing of 0.61 mm inside diameter. At each fixed radius the survey measurements were used to obtain the aftermixed conditions, where the flow was assumed to be at circumferentially uniform conditions (ref. 6). These mixed-out conditions and the calculated kinetic energy and total pressure losses for the vane are presented in table VI and figure 29. The overall kinetic energy loss coefficient for the vane was determined to be 0.041 (ref. 7).

Summary of Results

A laser anemometer was employed to experimentally determine the velocity and flow angle in the blade-to-blade plane within and downstream of a core turbine stator vane cascade. The use of fluorescent seed particles to track the airflow allowed the laser measurements to be made to within 1 mm of the vane and endwall surfaces. The laser measurements were performed in an ambient-air inlet, full-annular cascade operating near the design, mean-radius, exit, critical velocity ratio of 0.78. Surveys of velocity and flow angle obtained at constant axial positions within the vane passage (every 10 percent) and at 1/2 axial chord downstream of the vanes are presented for constant radial positions near the hub, mean, and tip of the vanes. Measurements used to check for flow repeatability, flow periodicity, and incomplete-signal biasing errors are also included. A detailed description of the cascade inlet and vane geometry is presented, as well as formerly reported measurements of inlet boundary layer, vane surface static pressures, and downstream flow conditions and losses. The experimental laser measurements are presented in both plot and tabulated form so that they can be conveniently used as a test case for three-dimensional turbomachinery computer programs. The results of this investigation are summarized as follows:

1. The experimental laser measurements generally agreed well with calculations from the inviscid quasi-three-dimensional computer programs MERIDL and TSONIC, an indication of the usefulness of this analytic approach. The best agreement usually occurred at the mean radius and near the vane inlet. The largest differences of the measurements from theory were near the endwalls and toward the vane exit, where viscous and secondary flow effects and measurement uncertainty would be expected to be the greatest. For all the measurements within the vane passage (except at 1 percent of axial chord and 2.5 and 97.5 percent of span), the average difference and standard deviation of the measurements from theory were calculated to be 1.3 ± 3.0 percent in velocity and $2.1° \pm 1.5°$ in flow angle.

2. A particle dynamics calculation for 1.2-μm-diameter particles (the probable size of seed particles detected in this investigation) indicated that the seed particles would generally track the airflow to within 2 percent in velocity and 1° in flow angle for most of the passage. However, differences of 2.5 to 4 percent in velocity and 2° to 3° in flow angle were calculated near the vane suction surface toward the vane inlet.

3. The experimental laser measurements were found to be repeatable and periodic within the accuracy of measuring the seed particle vector velocity, which was statistically estimated to be about 0.8 percent in velocity and 1.2° in flow angle. Because of the relatively low turbulence levels within the vane passage, incomplete-signal biasing errors were not observed in this investigation.

Lewis Research Center
National Aeronautics and Space Administration
Cleveland, Ohio, October 8, 1981

Appendix A
Symbols

$\mathbf{a}_f$ unit vector in plane of incident beams

$\bar{e}_M$ aftermixed kinetic energy loss coefficient at radius R, $1-(V/V_{id})^2_M$

h vane height, mm

I_j turbulence intensity, σ_j/V

m parameter in power-law boundary layer profile, eq. (6)

N number of fringes

n number of fringe orientation measurements or total number of measurements

p pressure, N/m^2

R radial position, percent of span

s fringe spacing, m

T temperature, K

$\mathbf{V}$ vector velocity, m/sec

V velocity magnitude, m/sec

V_j velocity component, m/sec

W mass flow, kg/sec

X, Y nondimensional coordinates

y distance normal to wall, mm

Z axial position, percent of axial chord

α flow angle measured from axial direction, deg

δ ratio of inlet total pressure to NACA standard pressure, p'_0/p'_{std}

δ_{bl} boundary layer thickness, mm

θ circumferential position, deg

θ_{cr} squared ratio of critical velocity at bellmouth inlet to critical velocity at NACA standard temperature, $V^2_{cr,0}/V^2_{cr,std}$

λ wavelength of laser light, m

σ_j standard deviation of velocity measurements, $\sqrt{\sum_{i=1}^{n} (V_i-\bar{V})^2/(n-1)}$, m/sec

τ_N transit time for a particle to travel N fringes, sec

φ_j angle of velocity component V_j with respect to axial direction, or fringe pattern orientation, deg

ψ angle between two focused laser beams, deg

Subscripts:

cr flow conditions at Mach 1

fs free stream

G gas (air)

h hub

id ideal or isentropic process

M mixed-out station; uniform flow in circumferential direction

m mean radius

P particle

p pressure surface

s suction surface

t tip

std NACA standard sea-level conditions (temperature equal to 288.2 K and pressure equal to 101 325 N/m^2)

0 station at inlet plane of cascade bellmouth, fig. 2

1 station upstream of vane, fig. 2

Superscripts:

$( )'$ total-state conditions

$(\hat{})$ least-squares value

$(\bar{})$ average value

Appendix B
Laser Anemometer System

This appendix includes a brief review of the theory of the fringe type of laser anemometer and a description of the optics, traversing mechanism, windows, seeding, and electronics used in the investigation.

Theory

The fringe type of laser anemometer is based on a set of interference fringes formed by focusing two laser beams into a common spatial region called the probe volume. These fringes are a set of parallel planes of constant-intensity light that are oriented such that their normals (with unit vector $\mathbf{a}_f$) lie in the plane of the two beams and are perpendicular to the bisector of the beams. The separation between the fringes is

$$s = \frac{\lambda}{2 \sin \psi/2} \tag{B1}$$

where λ is the wavelength of the laser light and ψ is the angle between the two focused beams.

As small particles entrained in the flow pass through the fringes in the probe volume, they scatter light as each bright fringe is crossed. Some of this scattered light is detected and processed to measure the transit time τ_N for a particle to travel a distance equal to N fringe spacings.

The velocity component measured V_j is the distance traveled by the particle divided by the time to travel that distance; that is,

$$V_j = \frac{Ns}{\tau_N} = \frac{N\lambda}{2\tau_N \sin \psi/2} \tag{B2}$$

This measured velocity component is related to the vector velocity of the particle $\mathbf{V}$ by

$$V_j = \mathbf{V} \cdot \mathbf{a}_f \tag{B3}$$

In general, measurement of three linearly independent velocity components can be used to calculate the vector velocity by inverting equation (B3). However, for the measurements presented in this report, only velocity components in the axial-tangential (blade to blade) plane could be measured because the optical axis was alined in the radial direction. Radial components of velocity, however, are expected to be small for the axial-flow turbine vanes tested herein.

Optics

Figure 6 shows the optical configuration. The argon-ion laser had an output power of about 1.5 W in a vertically polarized TEM_{00} mode at a wavelength of 0.5145 μm.

A beam splitter (described in ref. 10) was mounted in a remotely controlled rotary actuator. The output of the beam splitter consisted of two equal-intensity parallel beams that lay on a common circular path centered on the optical axis. The separation of the two parallel beams was about 1 cm.

The two parallel beams from the beam splitter were reflected by mirrors M_3 and M_4. Mirror M_4 was elliptical with a minor axis of 15.2 mm and a major axis of 21.6 mm. The parallel beams were focused by lens L_3 (200-mm focal length) to cross at the probe volume after being reflected by mirror M_5.

Light scattered by particles passing through the probe volume (after reflection from mirror M_5) was collimated by lens L_3, and the portion of this light not blocked by the elliptical mirror M_4 was focused by lens L_4 (160-mm focal length). A 100-μm-diameter pinhole aperture was located at the focal point. The diameter of the image of the aperture at the probe volume was equal to the $1/e^2$ diameter (125 μm) of the beams at the probe volume. This size pinhole was selected to minimize the amount of extraneous light incident on the photomultiplier tube.

A sharp cut-on colored glass filter was located in front of lens L_4 to block the green laser light at 0.5145 μm while passing the orange fluorescent radiation from the dye solution aerosol. This filter was 3 mm thick and had a 50-percent transmission wavelength of 0.530 μm.

The photomultiplier tube (PMT) was a type 4526 mounted in a housing with radiofrequency and magnetic shielding. The tube was selected to have a minimum quantum efficiency of 21 percent (at 0.5 μm).

The pinhole aperture was placed in an $x-y$ translation stage that was mounted on the PMT housing. The housing was, in turn, mounted on a linear translation stage that could be moved along the z axis (the optical axis). This three-axis positioning capability allowed the pinhole to be precisely set to achieve the best signal-to-noise ratio.

The focal lengths and positions of the two mode-matching lenses (L_1 and L_2) were selected to satisfy two criteria. First, the diameter of the beam waists in the probe volume was selected to give about 12 fringes between the $1/e^2$ intensity points. This number of fringes was chosen to maximize the signal-to-noise ratio while providing the minimum number of cycles (10) needed by the signal processor. (In general, the signal-to-noise ratio increases as the number of fringes, with a fixed spacing, decreases.)

The second criterion was that the beam waists must be at the crossing point of the beams in order to minimize fringe spacing gradients (ref. 16). The procedure used to select the mode-matching lenses is described in reference

5. The lenses selected for L_1 and L_2 had focal lengths of 160 and 127 mm, respectively. Because of the small beam diameter, simple lenses could be used for the mode-matching lenses.

The following procedure was used to insure that the mode-matching lenses were correctly located to meet these criteria. A collimator at the laser output was used to form a 25-mm-diameter collimated beam. The position of the beam waist after it passed through the mode-matching lenses was calculated for the collimated beam. (This is not the same position as waist position without the collimator, but it is much easier to measure because of the smaller f number of the beam.) After the first mode-matching lens was placed at its approximately proper position, the second lens was positioned so the beam waist was at its calculated position. This accurately fixed the separation between the lenses, which is more critical than the position of the lens pair. The collimator was then removed from the laser.

The focusing lenses L_3 and L_4 were 50.8-mm-diameter, cemented achromatic doublets corrected for spherical aberration (to third order) for an object-image ratio of infinity. A 20-mm-diameter, circular central mask was placed on the back surface of lens L_4 in order to reduce the depth of field of the receiving optics. This allowed measurements to be made closer to the hub and the window. The effective f number of the receiving optics (defined as the f number of optics without a central stop that would collect the same amount of light as the actual optics) was $f/5$.

Fringe spacing was determined to be 10.50 ± 0.03 μm by using equation (B1) with the measured value of the beam crossing angle ψ and the known wavelength λ. The crossing angle was determined by projecting the two beams on a screen located about 16 m from the probe volume and measuring their separation. An additional focusing lens was used between the laser and the first mode-matching lens during this procedure in order to reduce the size of the beams on the screen and thus increase the accuracy of the separation measurement.

This measurement of the fringe spacing was made without a window in the beam path. In operation the curved windows refracted the beams, causing a change in the fringe spacing. This change (less than 0.25 percent) was calculated by using ray-tracing methods and was used to correct the measured fringe spacing.

Traversing Mechanism

The laser and all the optics were mounted on a rigid plate that rested on two other plates (fig. 6). The top plate, called the radial motion plate, could be moved in a radial direction to position the probe volume at the desired radius in the cascade. The center plate, called the circumferential plate, was designed to move in a circular arc about the axis of the cascade. This permitted the probe volume to make circumferential surveys of the test region at a fixed radius. Most of the data presented in this report were taken this way. The third (bottom) plate, called the axial motion plate, could be moved parallel to the axis of the cascade to set the probe volume at the desired axial plane.

In addition to these three motions the probe volume position could be adjusted by using mirror M_5, called the tilting mirror, which was mounted in a two-axis gimbal mount. This allowed the optical axis of the beams to be moved about $\pm 10°$ in both the vertical and horizontal directions. The purpose of the tilting mirror was to permit measurements to be made close to the vane surfaces. (With the beam optical axis restricted to a radial line the measurement region in the cascade would be limited by one or both of the incident beams intersecting a vane surface before reaching the probe volume position.)

The radial motion plate, the circumferential motion plate, the beam splitter orientation, and the tilting mirror were remotely positioned. The axial motion plate was manually positioned. Position transducers were used to measure the positions of each of these, and these data were used to calculate and control the position of the probe volume.

Windows

Two windows were used. One, made of 3.175-mm-thick clear acrylic plastic, was located downstream of the vane row. It was a 27-cm-by-4-cm piece of flat material that was bent and held in place by a frame so that its inner surface matched the tip wall radius. The circumferential viewing range was about 56°. This acrylic plastic window, however, was damaged by the intensely focused laser beams. The damage showed up as a thin, scribed line on the window surface and occurred when the probe volume was close to the window.

The second window was located at the vane row (fig. 4) to permit measurements within the vane passage. This window was made from glass and did not experience the problems encountered with the acrylic plastic window.

The glass window covered about 39° in the circumferential direction, was 4 cm high, and was 3.175 mm thick. The glass was formed into a cylindrical shape that matched the tip radius by sagging it, in a vacuum furnace, onto a machined graphite form. The form was designed so that the window area used for measurements did not touch the form during the sagging process. (Areas of the glass that touched the form would pick up the small imperfections in the form that would degrade the optical transmission properties.)

The vanes at the glass window were machined to the tip radius. A silicone rubber sealing material was used to seal both windows to the cascade housing and to seal the vane tips to the glass window.

Seeding

A fluorescent dye aerosol was used as the seed material for these tests. This technique (described in ref. 17) was used to allow measurements to be made close to the hub, the vanes, and the windows.

A liquid dye solution (0.02 molar solution of rhodamine 6G in a 50-50 mixture, by volume, of benzyl alcohol and ethylene glycol) was atomized in a commercial aerosol generator. For some of the tests the aerosol from the atomizer was passed through an evaporation-condensation generator before injection into the flow upstream of the test section.

The size of the particles actually involved or detected in the laser anemometer measurement process (hereinafter referred to as the detected particles) is extremely important because the difference between the detected particle velocity (which is measured) and the true gas velocity is a strong function of particle size. This difference directly contributes to the error in the measurement of the gas velocity. However, it is difficult to directly determine the size of the detected particles. One contributing factor is that the particle generator produces a distribution of particle sizes. Another is that the laser anemometer can only detect particles larger than some minimum size. This minimum size is dependent on the factors that contribute to the signal amplitude and to the signal-to-noise ratio. These factors are the particle velocity, the laser power, the signal processor threshold setting, the PMT supply voltage, and the amount of extraneous light scattered from surfaces that reaches the PMT. The actual size distribution of the detected particles thus ranges from some unknown lower limit to the maximum size produced by the seed generator.

Three independent estimates of the mean diameter of the detected particles were obtained. One estimate was made by using the laser anemometer to measure the velocity distribution of particles at the exit of a sonic nozzle. The particle velocity, as a function of particle diameter, was calculated by assuming isentropic flow and the Stokes drag relation. The distribution of particle diameters detected with the laser anemometer was then determined by matching the measured velocities with the calculated velocities. For the same PMT supply voltage, signal processor threshold, and laser power, the mean particle diameter was found to be about 1.2 μm. However, there were two differences between the nozzle measurements and the cascade measurements. First, the nozzle measurements were taken at a higher velocity than the cascade measurements. Because the minimum detectable particle size increases with velocity, the nozzle measurements would give a larger mean particle diameter. The second difference was that the nozzle measurements were not taken close to any surfaces that could scatter light into the receiving optics. The greater amount of such extraneous light in the cascade measurements would tend to raise the mean detected particle diameter for measurements taken close to the vane surfaces and the endwalls.

A second independent estimate of the detected particle size was made as follows: The velocity of the particles, as a function of particle diameter, was calculated (by using the procedure described in the section *Seed particle velocity*) at the 20-percent-of-axial-chord plane for tangential locations within three degrees of the suction surface. This region was chosen because of the relatively large deviations between the particle and gas velocities. The detected particle mean diameter was then determined by matching the relative difference between the calculated particle velocity and the calculated gas velocity to the relative difference between the measured particle velocity and the calculated gas velocity. This procedure gave a mean particle diameter of 1.3 μm.

The final estimate of the detected particle size was taken from measurements made with a similar laser anemometer and reported in reference 11. In that work the measured particle velocity downstream of a rotor passage shock was used to calculate the mean detected particle diameter. The value obtained for the mean particle diameter was 1.4 μm.

From these particle size measurements, it was estimated that the mean detected particle diameters for the cascade measurements were in the range 1.1 to 1.4 μm, with a typical diameter of 1.2 μm. The mean diameter was probably somewhat larger than this typical value for measurements made within about 3 mm of surfaces. On the other hand, for lower velocity measurements not near surfaces, the mean diameter could have been somewhat less than this typical value. Also, the evaporation-condensation generator, which was used for many of the cascade measurements, may have produced an aerosol with a narrower size distribution. This would have resulted in a smaller detected mean diameter. However, no measurements were made to check this. One effect of the evaporation-condensation generator was to decrease the data rate of the measurements. For this reason it was not used for all the measurements presented in this report (table III).

Electronics and Data Processing

A microcomputer, based on an 8080 central processing unit, was used for collecting data and for controlling the traversing mechanism. It was also used to generate on-line data displays so that the system could be monitored for proper operation.

The signal from the PMT was processed by a commercial, counter type of processor designed for use with the fringe type of laser anemometer signal. This processor used a 500-MHz clock to measure the duration of eight cycles of the filtered burst signal. The filter cutoff frequencies (low pass and high pass) are given in

table III. Both 5/8 comparison and amplitude sequence validation methods were used for all measurements. The digital time interval data from the processor were sent to the microcomputer, which calculated the mean velocity and relative standard deviation for a fixed number (1000) of validated bursts.

The positions of the radial and circumferential motion plates and the tilting mirror and the orientation of the beam splitter were all controlled by the microcomputer. Data input to the microcomputer from the position transducers were used to calculate the actual position of the probe volume within the cascade. At each probe volume position, two velocity components (corresponding to two beam splitter orientations) were measured. The mean and the standard deviation for each velocity component, along with data that defined the position of the probe volume, the orientation of the beam splitter, the setting pressure of the cascade, and the total temperature, were recorded by the microcomputer.

As the data were recorded, they could also be displayed on a cathode ray tube display and on a printing terminal (a block diagram of the system is shown in fig. 7). This allowed the entire laser anemometer system to be monitored for proper operation during the experiment. Finally the data stored in the microcomputer memory were transmitted over a telephone line to the central computing facility for further processing.

References

1. Moffitt, Thomas P.; Stepka, Francis S.; and Rohlik, Harold E.: Summary of NASA Aerodynamic and Heat Transfer Studies in Turbine Vanes and Blades. SAE Paper 760917, Nov. 1976. (Also NASA TM X-73518, 1976.)
2. Lakshmiharayana, B.; and Runstadler, P., Jr., eds.: Measurement Methods in Rotating Components of Turbomachinery, Proceedings of the Joint Fluids Engineering Gas Turbine Conference and Products Show, American Society of Mechanical Engineers, 1980.
3. Katsanis, Theodore; and McNally, William D.: Revised FORTRAN Program for Calculating Velocities and Streamlines on the Hub-Shroud Midchannel Stream Surface of an Axial-, Radial-, or Mixed-Flow Turbomachine or Annular Duct. I: User's Manual. NASA TN D-8430, 1977.
4. Katsanis, Theodore: FORTRAN Program for Calculating Transonic Velocities on a Blade-to-Blade Stream Surface of a Turbomachine. NASA TN D-5427, 1969.
5. Seasholtz, Richard G.: Laser Doppler Velocimeter System for Turbine Stator Cascade Studies and Analysis of Statistical Biasing Errors. NASA TN D-8297, 1977.
6. Goldman, Louis J.; and McLallin, Kerry L.: Effect of Endwall Cooling on Secondary Flows in Turbine Stator Vanes. Secondary Flows in Turbomachines. AGARD CP-214, 1977, pp. 15-1—15-29. (Also NASA TM X-73568, 1977.)
7. Goldman, Louis J.; and McLallin, Kerry L.: Cold-Air Annular-Cascade Investigation of Aerodynamic Performance of Core-Engine-Cooled Turbine Vanes. I: Solid-Vane Performance and Facility Description. NASA TM X-3224, 1975.
8. Szanca, Edward M.; Schum, Harold J.; and Hotz, Glenn M.: Research Turbine for High-Temperature Core Engine Application. I: Cold-Air Overall Performance of Solid Scaled Turbine. NASA TN D-7557, 1974.
9. Goldman, Louis J.; Seasholtz, Richard G.; and McLallin, Kerry L.: Velocity Surveys in a Turbine Stator Annular-Cascade Facility Using Laser Doppler Techniques. NASA TN D-8269, 1976.
10. Powell, J. Anthony; Strazisar, Anthony J.; and Seasholtz, Richard G.: Efficient Laser Anemometer for Intra-Rotor Flow Mapping in Turbomachiney. Measurement Methods in Rotating Components of Turbomachinery, Proceedings of the Joint Fluids Engineering Gas Turbine Conference and Products Show, American Society of Mechanical Engineers, 1980, pp. 157-164. (Also NASA TM-79320, 1979.)
11. Strazisar, Anthony J.; and Powell, J. Anthony: Laser Anemometer Measurements in a Transonic Axial Flow Compressor Rotor. Measurement Methods in Rotating Components of Turbomachinery, Proceedings of the Joint Fluids Engineering Gas Turbine Conference and Products Show, American Society of Mechanical Engineers, 1980, pp. 165-176. (Also NASA TM-79323, 1979.)
12. Wolberg, John R.: Prediction Analysis. D. Van Nostrand, 1967.
13. Kline, S. J.; and McClintock, F. A.: Describing Uncertainties in Single-Sample Experiments. Mech. Eng., vol. 75, no. 1, Jan. 1953, pp. 3-8.
14. Boyle, Robert J.; Rohlik, Harold E.; and Goldman, Louis J.: Analytic Investigation of Effect of End-Wall Contouring on Stator Performance. NASA TP-1943, 1981.
15. Maxwell, Barry R.: Particle Flow in Turbomachinery with Application to Laser-Doppler Velocimetry. AIAA J., vol. 12, no. 10, Oct. 1974, pp. 1297-1298.
16. Hanson, S.: Broadening of the Measured Frequency Spectrum in a Differential Laser Anemometer due to Interference Plane Gradients. J. Phys. D., vol. 6, no. 1, Jan. 1973, pp. 164-171.
17. Stevenson, W. H.; dos Santos, R.; and Mettler, S. C.: A Laser Velocimeter Utilizing Laser-Induced Fluoresence. Appl. Phys. Lett., vol. 27, no. 7, Oct. 1975, pp. 395-396.

TABLE I. - LASER ANEMOMETER MEASUREMENT UNCERTAINTIES

Quantity	Uncertainty[a]
Axial position, Z, percent of axial chord	±0.4, $Z \leq 80$ percent ±0.9, $Z > 80$ percent
Radial position, R, percent of span	±0.6
Circumferential position, θ, deg	±0.2
Velocity component measurement angle, φ_j, deg	±0.3
Velocity component, V_j, percent	±1.0
Velocity magnitude, V, percent	±0.8
Flow angle, α, deg	±1.2
Turbulence intensity, I_j, percent	±10

[a]For 95-percent confidence interval.

TABLE II. - LASER VELOCITY MEASUREMENTS AT CONSTANT AXIAL AND RADIAL POSITIONS WITHIN AND DOWNSTREAM OF CORE TURBINE STATOR VANES

Data point	Run																											
	1							2							3							4						
	Axial position, Z, percent of axial chord from leading edge																											
	1.3							10.2							10.2							10.2						
	Radial position, R, percent of span from hub																											
	50.2							9.9							50.2							90.1						
	Velocity component measurement angles, deg																											
	φ_1 = -44.9, -44.9, -29.3, -6.6 φ_2 = -0.4, 14.8, 10.3, 41.2 N = 1, 2-6, 7-17, 18-23							φ_1 = -25.1, -9.9 φ_2 = 15.0, 25.9 N = 1-8, 9-17							φ_1 = -24.8, -10.0 φ_2 = 15.0, 30.0 N = 1-15, 16-24							φ_1 = -25.0, -10.1 φ_2 = 14.9, 30.0 N = 1-11, 12-22						
	Circumferential position, θ, deg	Component critical velocity ratios		Component turbulent intensities, percent		Critical velocity ratio, V/V_{cr}	Flow angle, α, deg	Circumferential position, θ, deg	Component critical velocity ratios		Component turbulent intensities, percent		Critical velocity ratio, V/V_{cr}	Flow angle, α, deg	Circumferential position, θ, deg	Component critical velocity ratios		Component turbulent intensities, percent		Critical velocity ratio, V/V_{cr}	Flow angle, α, deg	Circumferential position, θ, deg	Component critical velocity ratios		Component turbulent intensities, percent		Critical velocity ratio, V/V_{cr}	Flow angle, α, deg
		V_1/V_{cr}	V_2/V_{cr}	σ_1/V	σ_2/V				V_1/V_{cr}	V_2/V_{cr}	σ_1/V	σ_2/V				V_1/V_{cr}	V_2/V_{cr}	σ_1/V	σ_2/V				V_1/V_{cr}	V_2/V_{cr}	σ_1/V	σ_2/V		
1	23.4	.267	.164	5.9	4.5	.270	-53.0	21.9	.438	.377	2.6	4.4	.443	-16.7	22.6	.453	.400	4.0	4.4	.460	-14.7	23.5	.483	.411	3.1	3.6	.487	-17.4
2	23.1	.299	.201	5.5	4.5	.304	-33.8	21.5	.379	.366	2.6	2.9	.397	-7.8	22.3	.416	.396	3.8	3.3	.433	-8.6	23.1	.445	.415	2.3	2.8	.460	-10.4
3	22.7	.302	.247	5.1	3.3	.321	-25.0	21.2	.355	.358	2.3	2.7	.380	-4.4	22.0	.383	.387	2.3	2.4	.409	-4.2	22.7	.412	.405	2.5	2.5	.435	-6.4
4	22.4	.285	.276	3.8	6.5	.323	-16.7	20.9	.330	.350	2.4	2.4	.363	-0.6	21.6	.359	.378	2.8	2.2	.393	- .9	22.4	.388	.399	2.5	2.4	.419	-3.0
5	22.0	.268	.281	3.6	4.1	.317	-12.7	20.5	.310	.342	2.4	2.2	.350	2.7	21.3	.331	.366	2.7	2.4	.374	2.9	22.1	.361	.387	2.5	2.4	.400	.5
6	21.7	.257	.299	3.0	3.6	.324	-7.6	20.2	.293	.335	2.3	2.3	.340	5.3	20.9	.311	.356	2.5	2.6	.361	5.6	21.7	.340	.377	2.6	2.5	.385	3.0
7	21.3	.289	.298	3.9	5.2	.313	-7.2	19.8	.277	.321	2.3	2.4	.324	6.2	20.6	.293	.345	2.3	2.7	.348	7.9	21.4	.318	.366	2.7	2.6	.370	6.0
8	21.0	.277	.310	3.1	3.7	.316	- .5	19.5	.262	.312	2.2	2.4	.314	8.2	20.2	.277	.335	2.2	2.3	.336	9.8	21.0	.302	.356	2.4	2.5	.359	7.6
9	20.7	.266	.305	2.8	2.8	.308	1.3	19.1	.282	.288	2.1	2.2	.303	11.8	19.9	.265	.327	2.1	2.4	.327	11.2	20.7	.286	.345	2.5	2.5	.347	9.3
10	20.3	.256	.299	2.4	2.8	.302	2.6	18.8	.272	.280	2.0	2.5	.294	12.3	19.6	.252	.313	2.3	2.4	.313	11.7	20.4	.273	.334	2.4	2.6	.335	10.5
11	20.0	.246	.296	2.4	3.2	.297	4.9	18.4	.262	.278	2.0	2.3	.288	14.8	19.2	.238	.303	2.3	2.3	.303	13.5	20.0	.259	.324	2.5	2.8	.324	12.0
12	19.6	.234	.292	2.5	2.6	.292	7.5	18.1	.248	.270	2.1	2.3	.277	16.5	18.9	.225	.292	2.4	2.4	.292	14.9	20.0	.299	.307	2.4	2.6	.323	12.0
13	19.2	.224	.277	4.8	4.1	.278	6.8	17.8	.237	.261	2.0	2.4	.267	17.5	18.5	.212	.282	2.4	2.4	.282	16.4	19.6	.284	.300	2.6	2.5	.312	14.0
14	18.9	.215	.271	2.5	3.0	.271	8.2	17.4	.228	.254	2.1	2.5	.259	18.4	18.2	.203	.274	2.8	2.5	.274	17.4	19.3	.274	.292	2.5	2.6	.302	14.7
15	18.6	.205	.268	2.4	2.5	.268	11.0	17.1	.220	.248	2.3	2.7	.252	19.5	17.8	.193	.266	2.4	2.4	.266	18.7	19.0	.263	.283	2.7	2.8	.292	15.5
16	18.2	.197	.262	2.5	2.4	.262	12.1	16.7	.211	.240	2.5	2.9	.244	20.1	19.2	.276	.290	2.0	2.6	.302	13.9	18.6	.250	.276	2.6	2.6	.283	17.5
17	17.9	.187	.253	2.5	2.5	.254	13.1	16.4	.202	.237	2.5	4.0	.239	22.3	18.8	.263	.283	2.0	2.3	.292	15.7	18.3	.240	.267	2.9	2.9	.273	18.1
18	17.5	.230	.224	2.3	8.4	.248	15.6								18.5	.250	.275	---	2.4	.282	17.4	17.9	.232	.261	3.0	2.9	.265	19.1
19	17.2	.222	.217	---	3.3	.240	15.8								18.2	.241	.267	2.2	2.4	.273	18.0	17.6	.220	.253	2.9	3.4	.257	20.8
20	16.8	.210	.213	2.4	3.6	.232	18.1								17.8	.230	.259	2.1	2.7	.264	19.2	17.3	.214	.246	3.2	3.2	.249	20.8
21	16.5	.202	.206	2.6	3.8	.223	18.6								17.5	.219	.252	2.3	2.7	.255	20.7	16.9	.209	.246	3.2	3.5	.248	22.8
22	16.2	.190	.199	3.5	4.3	.213	20.1								17.1	.215	.245	2.6	---	.249	20.0	16.6	.200	.238	3.8	3.8	.240	23.3
23	15.8	.171	.190	5.4	5.7	.199	24.1								16.8	.203	.238	3.6	3.1	.240	22.2							
24															16.4	.197	.232	3.9	3.4	.234	22.7							

Table II. - Continued.

Data point	Run																									
	5							6							7						8					
	Axial position, Z, percent of axial chord from leading edge																									
	20.0							20.0							20.0						20.0					
	Radial position, R, percent of span from hub																									
	2.3							9.7							9.9						49.4					
	Velocity component measurement angles, deg																									
	φ_1 = -10.6 φ_2 = 39.9 N = 1-18							φ_1 = -10.7 φ_2 = 39.9 N = 1-16							φ_1 = -10.0 φ_2 = 39.8 N = 1-16						φ_1 = -10.5 φ_2 = 39.9 N = 1-19					
	Circumferential position, θ, deg	Component critical velocity ratios		Component turbulent intensities, percent		Critical velocity ratio, V/V_{cr}	Flow angle, α, deg	Circumferential position, θ, deg	Component critical velocity ratios		Component turbulent intensities, percent		Critical velocity ratio, V/V_{cr}	Flow angle, α, deg	Circumferential position, θ, deg	Component critical velocity ratios		Component turbulent intensities, percent		Critical velocity ratio, V/V_{cr}	Flow angle, α, deg	Circumferential position, θ, deg	Component critical velocity ratios		Component turbulent intensities, percent		Critical velocity ratio, V/V_{cr}	Flow angle, α, deg
		V_1/V_{cr}	V_2/V_{cr}	σ_1/V	σ_2/V				V_1/V_{cr}	V_2/V_{cr}	σ_1/V	σ_2/V				V_1/V_{cr}	V_2/V_{cr}	σ_1/V	σ_2/V				V_1/V_{cr}	V_2/V_{cr}	σ_1/V	σ_2/V		
1	21.6	.470	.412	3.2	2.7	.492	6.7	21.9	.526	.423	2.4	---	.538	1.6	22.1	.542	.419	3.2	2.7	.550	-0.5	22.7	.575	.450	2.7	2.5	.585	0.1
2	21.3	.435	.415	2.9	11.6	.470	11.8	21.6	.473	.402	2.2	2.5	.491	4.8	21.7	.487	.392	2.4	3.3	.498	1.8	22.4	.521	.433	2.9	2.4	.537	3.6
3	20.9	.403	.366	3.3	3.1	.428	8.8	21.3	.442	.388	2.1	2.6	.463	6.6	21.4	.449	.375	2.2	2.8	.463	4.0	22.0	.471	.409	2.3	2.5	.492	6.2
4	20.6	.376	.395	3.8	17.3	.427	17.6	20.9	.411	.373	2.3	2.5	.436	8.7	21.0	.419	.373	2.4	2.7	.440	7.8	21.6	.437	.394	2.4	2.5	.462	8.3
5	20.2	.344	.333	8.5	4.9	.374	12.6	20.6	.381	.358	2.4	2.5	.409	10.8	20.7	.389	.357	2.4	2.9	.413	9.7	21.3	.411	.377	2.3	2.6	.437	9.5
6	21.0	.408	.369	4.1	3.8	.432	8.5	20.2	.354	.344	2.3	2.4	.386	12.8	20.3	.363	.345	2.3	2.5	.393	11.9	20.9	.383	.363	2.4	2.5	.413	11.3
7	20.7	.378	.355	4.7	4.6	.406	11.0	19.9	.331	.333	2.3	2.6	.367	15.0	20.0	.344	.336	2.5	2.5	.375	13.6	20.6	.357	.350	2.6	2.6	.391	13.3
8	20.3	.334	.327	8.4	6.5	.365	13.3	19.6	.313	.322	2.4	2.6	.351	16.4	19.7	.322	.326	2.5	7.8	.357	15.8	20.6	.357	.347	2.6	2.4	.389	12.9
9	20.0	.323	.330	6.8	6.3	.361	15.9	19.2	.294	.310	2.4	2.3	.335	17.7	19.3	.302	.316	2.4	2.7	.341	17.7	20.3	.334	.340	2.3	2.6	.373	15.7
10	19.6	.310	.326	4.3	4.8	.352	17.8	18.9	.279	.303	2.2	2.4	.323	19.5	19.0	.285	.309	2.5	4.1	.329	19.8	19.9	.311	.328	2.6	2.5	.354	17.7
11	19.3	.298	.318	3.8	3.4	.341	18.6	18.5	.264	.293	2.2	2.6	.310	20.9	18.6	.275	.298	2.4	2.5	.318	19.9	19.6	.299	.316	2.4	2.8	.340	18.1
12	18.9	.279	.304	4.7	4.0	.324	19.7	18.2	.251	.285	2.2	2.7	.299	22.4	18.3	.255	.283	9.6	5.6	.299	21.3	19.2	.282	.306	2.3	2.7	.326	19.5
13	18.6	.269	.295	3.5	3.5	.313	20.0	17.8	.239	.278	2.5	2.7	.290	23.7	17.9	.251	.277	2.7	10.4	.293	21.0	18.9	.266	.296	2.3	2.7	.312	21.1
14	18.2	.253	.288	2.8	3.7	.302	22.5	17.5	.227	.270	2.6	3.0	.279	24.7	17.6	.233	.271	2.2	2.7	.281	24.1	18.5	.252	.288	2.4	2.6	.302	22.7
15	17.9	.243	.279	3.5	3.2	.292	23.0	17.1	.217	.256	2.6	3.1	.266	24.5	17.2	.224	.261	2.3	2.8	.271	24.3	18.2	.239	.279	2.6	2.6	.290	24.0
16	17.5	.230	.272	4.0	3.9	.282	24.6	16.7	.207	.249	2.8	3.0	.257	25.6	16.9	.210	.255	2.7	12.0	.262	26.7	17.8	.228	.270	2.8	3.0	.279	24.8
17	17.2	.224	.269	3.5	3.5	.277	25.5															17.5	.225	.262	3.4	2.9	.273	23.9
18	16.8	.208	.254	4.9	3.5	.261	26.5															17.1	.206	.252	2.9	3.1	.259	26.7
19																						16.8	.199	.245	2.9	3.1	.251	27.2

TABLE II. - Continued.

Data point	Run																												
	9							10							11							12								
	Axial position, Z, percent of axial chord from leading edge																												
	20.0							20.0							20.0							20.0								
	Radial position, R, percent of span from hub																												
	49.8							90.1							90.1							97.4								
	Velocity component measurement angles, deg																												
	φ_1 = -10.1 φ_2 = 39.8 N = 1-18							φ_1 = -10.7 φ_2 = 39.9 N = 1-20							φ_1 = -10.2 φ_2 = 29.7 N = 1-19							φ_1 = -10.2 φ_2 = 30.1 N = 1-17								
	Circumferential position, θ, deg	Component critical velocity ratios		Component turbulent intensities, percent		Critical velocity ratio, V/V_{cr}	Flow angle, α, deg	Circumferential position, θ, deg	Component critical velocity ratios		Component turbulent intensities, percent		Critical velocity ratio, V/V_{cr}	Flow angle, α, deg	Circumferential position, θ, deg	Component critical velocity ratios		Component turbulent intensities, percent		Critical velocity ratio, V/V_{cr}	Flow angle, α, deg	Circumferential position, θ, deg	Component critical velocity ratios		Component turbulent intensities, percent		Critical velocity ratio, V/V_{cr}	Flow angle, α, deg
		V_1/V_{cr}	V_2/V_{cr}	σ_1/V	σ_2/V				V_1/V_{cr}	V_2/V_{cr}	σ_1/V	σ_2/V				V_1/V_{cr}	V_2/V_{cr}	σ_1/V	σ_2/V				V_1/V_{cr}	V_2/V_{cr}	σ_1/V	σ_2/V		
1	22.8	.588	.456	2.3	3.0	.597	-0.3	23.2	.605	.471	2.8	2.7	.615	-0.2	23.3	.646	.580	3.4	3.3	.660	1.3	23.6	.631	.545	4.8	4.9	.639	-1.4
2	22.4	.537	.431	2.5	2.3	.548	1.6	22.9	.535	.442	2.9	2.4	.551	3.2	22.9	.525	.478	3.0	2.9	.538	2.5	23.2	.562	.501	3.5	4.0	.573	1.0
3	22.1	.488	.414	2.3	2.1	.505	4.8	22.5	.487	.426	3.0	2.6	.510	6.6	22.6	.484	.460	2.7	2.5	.504	5.7	22.9	.511	.469	3.7	3.3	.526	3.4
4	21.7	.445	.395	2.1	2.3	.468	7.5	22.2	.453	.411	2.5	3.0	.480	8.6	22.2	.452	.438	2.3	2.5	.474	7.1	22.5	.470	.450	3.2	3.1	.491	6.7
5	21.4	.419	.383	2.0	2.3	.444	9.2	21.8	.424	.399	2.6	3.2	.456	10.9	21.9	.418	.415	2.6	2.6	.443	9.3	22.2	.437	.429	3.4	2.9	.462	8.5
6	21.0	.390	.366	2.2	4.0	.418	11.0	21.5	.400	.377	3.3	3.0	.431	11.0	21.5	.394	.399	2.7	2.8	.422	10.7	21.8	.412	.414	3.3	3.3	.440	10.2
7	20.7	.364	.355	2.2	2.2	.397	13.2	21.1	.376	.363	2.6	2.7	.409	12.6	21.2	.374	.384	2.8	2.8	.403	11.9	21.5	.386	.399	4.4	3.5	.418	12.5
8	20.3	.342	.342	2.2	2.4	.377	14.9	20.8	.355	.351	2.8	2.8	.390	14.0	20.8	.342	.369	2.9	2.8	.380	15.9	21.5	.379	.390	5.5	5.8	.410	12.2
9	20.0	.321	.332	2.2	5.2	.360	16.8	20.5	.334	.337	2.9	2.9	.371	15.1	20.5	.324	.357	3.1	3.1	.366	17.4	21.1	.354	.376	5.5	6.4	.391	14.6
10	19.7	.305	.320	2.1	2.5	.345	17.8	20.1	.313	.324	2.9	3.0	.353	16.7	20.1	.305	.342	2.8	2.8	.349	18.6	20.8	.330	.364	6.2	6.4	.373	17.4
11	19.3	.289	.309	2.3	2.4	.331	18.9	19.8	.298	.314	2.7	3.0	.339	17.6	19.8	.292	.332	2.9	3.1	.337	19.6	20.5	.314	.344	5.5	6.4	.353	17.2
12	19.0	.275	.301	2.1	2.5	.319	20.5	19.4	.283	.305	2.8	2.7	.326	19.1	19.4	.277	.318	2.8	3.1	.322	20.4	20.1	.298	.335	4.6	6.1	.342	18.9
13	18.6	.256	.292	2.2	2.6	.305	22.7	19.1	.270	.295	2.8	2.8	.313	19.8	19.1	.267	.309	2.9	3.1	.312	20.9	19.8	.284	.314	4.9	7.5	.321	17.8
14	18.3	.248	.284	9.3	10.9	.296	23.0	18.7	.258	.286	2.8	2.8	.302	20.8	18.7	.258	.300	2.9	3.1	.303	21.4	19.4	.270	.305	4.4	6.9	.311	19.3
15	17.9	.235	.272	2.3	2.6	.283	23.9	18.4	.246	.279	2.9	2.9	.293	22.0	18.4	.244	.285	3.0	3.0	.288	21.9	19.1	.257	.297	4.4	6.1	.301	21.1
16	17.6	.224	.263	4.4	2.8	.272	24.5	18.0	.232	.269	3.1	2.7	.280	23.4	18.1	.230	.278	3.5	3.1	.279	24.2	18.7	.245	.284	4.9	6.7	.287	21.2
17	17.2	.211	.254	8.9	2.8	.261	26.0	17.7	.223	.260	3.4	3.1	.270	23.7	17.7	.216	.267	3.2	3.2	.268	25.8	18.4	.236	.277	4.6	5.6	.280	22.1
18	16.9	.205	.248	7.3	5.6	.255	26.2	17.4	.211	.252	3.5	3.1	.260	25.2	17.3	.208	.256	3.4	3.2	.257	25.6							
19								17.0	.197	.241	3.1	3.2	.248	26.5	17.0	.194	.246	3.4	3.4	.246	27.8							
20								16.7	.192	.237	3.1	3.2	.243	27.1														

TABLE II. - Continued.

Data point	Run													
	13							14						
	Axial position, Z, percent of axial chord from leading edge													
	30.0							40.1						
	Radial position, R, percent of span from hub													
	50.2							9.9						
	Velocity component measurement angles, deg													
	φ_1 = 5.0 φ_2 = 44.9 N = 1-17							φ_1 = 17.0 φ_2 = 55.0 N = 1-14						
	Circumferential position, θ, deg	Component critical velocity ratios		Component turbulent intensities, percent		Critical velocity ratio, V/V_{cr}	Flow angle, α, deg	Circumferential position, θ, deg	Component critical velocity ratios		Component turbulent intensities, percent		Critical velocity ratio, V/V_{cr}	Flow angle, α, deg
		V_1/V_{cr}	V_2/V_{cr}	σ_1/V	σ_2/V				V_1/V_{cr}	V_2/V_{cr}	σ_1/V	σ_2/V		
1	22.8	.642	.559	2.7	3.3	.650	14.2	22.5	.665	.604	2.3	2.1	.678	28.0
2	22.4	.585	.498	3.2	4.8	.590	12.4	22.1	.623	.559	2.3	2.5	.632	27.1
3	22.1	.538	.476	3.0	3.5	.547	15.3	21.8	.579	.520	2.7	3.5	.588	27.1
4	21.7	.496	.448	2.6	3.4	.507	16.9	21.4	.541	.483	2.8	2.4	.549	26.6
5	21.4	.469	.431	2.7	2.9	.482	18.2	21.1	.511	.461	2.5	2.2	.520	27.6
6	21.1	.440	.414	2.5	2.6	.456	20.2	20.8	.480	.439	2.3	2.1	.490	28.7
7	20.7	.413	.393	2.5	3.2	.430	21.0	20.4	.453	.420	2.2	2.0	.464	29.8
8	20.3	.392	.378	2.5	2.9	.410	22.0	20.1	.430	.402	2.1	2.7	.442	30.4
9	20.0	.371	.363	2.7	3.4	.390	23.1	19.7	.408	.385	2.1	2.3	.421	31.3
10	19.7	.348	.347	2.4	3.2	.370	24.9	19.4	.386	.369	2.2	2.4	.400	32.2
11	19.3	.328	.334	2.5	3.1	.352	26.3	19.0	.366	.354	2.3	2.3	.381	33.1
12	19.0	.312	.322	2.5	3.1	.338	27.5	18.7	.348	.340	2.4	3.3	.364	34.0
13	18.6	.297	.309	2.5	3.0	.323	28.0	18.3	.329	.325	2.4	2.5	.345	35.0
14	18.3	.283	.299	2.3	2.9	.310	29.1	18.0	.311	.311	3.0	2.6	.329	35.9
15	17.9	.269	.288	2.3	3.0	.298	30.5							
16	17.6	.254	.275	2.5	2.8	.283	30.9							
17	17.2	.241	.267	2.8	2.8	.273	33.0							

Data point	Run													
	15							16						
	Axial position, Z, percent of axial chord from leading edge													
	40.1							40.0						
	Radial position, R, percent of span from hub													
	49.8							50.2						
	Velocity component measurement angles, deg													
	φ_1 = 15.0 φ_2 = 55.0 N = 1-16							φ_1 = 15.1 φ_2 = 55.1 N = 1-16						
	Circumferential position, θ, deg	Component critical velocity ratios		Component turbulent intensities, percent		Critical velocity ratio, V/V_{cr}	Flow angle, α, deg	Circumferential position, θ, deg	Component critical velocity ratios		Component turbulent intensities, percent		Critical velocity ratio, V/V_{cr}	Flow angle, α, deg
		V_1/V_{cr}	V_2/V_{cr}	σ_1/V	σ_2/V				V_1/V_{cr}	V_2/V_{cr}	σ_1/V	σ_2/V		
1	23.3	.746	.682	4.1	3.5	.766	28.0	23.3	.740	.673	3.8	3.6	.758	27.7
2	23.0	.682	.612	2.5	2.5	.697	26.5	23.0	.673	.602	2.5	3.1	.686	26.5
3	22.6	.635	.574	2.4	2.5	.649	27.1	22.6	.631	.522	2.8	6.1	.633	20.7
4	22.3	.597	.532	2.5	2.6	.608	26.0	22.3	.583	.503	3.2	4.8	.589	23.7
5	21.9	.554	.493	2.5	2.4	.564	25.9	21.9	.544	.479	3.2	4.0	.553	25.1
6	21.6	.519	.467	2.9	2.3	.530	26.9	21.6	.512	.453	3.2	3.2	.521	25.6
7	21.3	.486	.443	2.3	2.1	.499	27.7	21.2	.480	.429	2.8	3.4	.489	26.4
8	20.9	.462	.424	2.3	2.8	.475	28.4	20.9	.457	.417	2.6	2.9	.468	28.0
9	20.6	.436	.405	2.1	2.5	.450	29.2	20.6	.434	.397	2.5	3.1	.446	28.2
10	20.2	.414	.388	2.7	2.7	.428	30.0	20.2	.412	.378	2.4	3.5	.423	28.4
11	19.9	.392	.372	2.2	2.6	.407	30.8	19.9	.390	.365	2.8	3.4	.404	30.0
12	19.5	.371	.358	5.3	5.3	.388	32.2	19.5	.367	.350	2.7	3.5	.382	31.4
13	19.2	.358	.351	10.5	9.0	.377	33.5	19.2	.349	.338	2.7	3.5	.366	32.7
14	18.8	.334	.331	9.2	2.2	.354	34.1	18.8	.327	.322	2.6	3.2	.345	34.1
15	18.5	.313	.316	2.4	3.1	.335	36.0	18.5	.309	.310	2.6	2.6	.329	35.3
16	18.2	.298	.305	5.3	3.3	.321	36.8	18.1	.292	.297	2.3	2.9	.314	36.5
17														

Table II. - Continued.

Data point	Run																													
	17							18							19							20						
	Axial position, Z, percent of axial chord from leading edge																													
	40.1							50.0							50.0							50.0						
	Radial position, R, percent of span from hub																													
	90.1							10.3							50.0							50.2						
	Velocity component measurement angles, deg																													
	φ_1 = 16.9 φ_2 = 55.0 N = 1-18							φ_1 = 20.0 φ_2 = 60.2 N = 1-13							φ_1 = 20.0 φ_2 = 60.2 N = 1-15							φ_1 = 20.1 φ_2 = 59.9 N = 1-15						
	Circumferential position, θ, deg	Component critical velocity ratios		Component turbulent intensities, percent		Critical velocity ratio, V/V_{cr}	Flow angle, α, deg	Circumferential position, θ, deg	Component critical velocity ratios		Component turbulent intensities, percent		Critical velocity ratio, V/V_{cr}	Flow angle, α, deg	Circumferential position, θ, deg	Component critical velocity ratios		Component turbulent intensities, percent		Critical velocity ratio, V/V_{cr}	Flow angle, α, deg	Circumferential position, θ, deg	Component critical velocity ratios		Component turbulent intensities, percent		Critical velocity ratio, V/V_{cr}	Flow angle, α, deg
		V_1/V_{cr}	V_2/V_{cr}	σ_1/V	σ_2/V				V_1/V_{cr}	V_2/V_{cr}	σ_1/V	σ_2/V				V_1/V_{cr}	V_2/V_{cr}	σ_1/V	σ_2/V				V_1/V_{cr}	V_2/V_{cr}	σ_1/V	σ_2/V		
1	23.9	.806	.726	7.0	6.7	.820	27.3	23.1	.703	.696	3.5	3.0	.745	39.3	23.6	.741	.729	6.4	6.1	.783	38.8	23.7	.745	.737	5.2	4.5	.788	39.1
2	23.6	.753	.663	3.2	2.6	.761	25.6	22.7	.662	.637	2.4	2.9	.692	37.1	23.3	.700	.674	3.9	4.2	.732	37.1	23.4	.700	.667	2.9	3.8	.729	36.2
3	23.3	.686	.605	2.8	2.4	.694	25.7	22.4	.633	.606	2.6	2.9	.661	36.7	23.0	.662	.624	3.2	3.7	.687	35.5	23.0	.671	.619	3.3	4.1	.690	33.7
4	22.9	.635	.557	2.6	2.9	.642	25.2	22.0	.604	.567	2.6	3.4	.626	35.2	22.6	.628	.596	3.4	3.4	.653	36.0	22.7	.628	.587	2.9	4.0	.649	34.8
5	22.6	.597	.519	2.6	2.8	.602	24.6	21.7	.571	.536	2.6	3.0	.592	35.2	22.3	.588	.550	3.6	4.7	.609	34.8	22.3	.595	.540	2.9	5.1	.609	32.4
6	22.2	.555	.482	2.6	2.6	.560	24.4	21.4	.549	.504	2.8	3.9	.564	33.4	21.9	.560	.521	3.4	4.4	.578	34.3	22.0	.564	.518	3.1	4.0	.579	33.4
7	21.9	.530	.455	2.6	2.0	.534	23.5	21.0	.510	.478	2.6	3.0	.529	35.0	21.6	.526	.485	4.0	4.6	.542	33.7	21.6	.524	.482	3.2	4.8	.539	33.3
8	21.5	.490	.434	2.4	2.2	.496	26.0	20.7	.478	.454	2.8	3.0	.497	36.0	21.3	.491	.455	4.7	4.3	.506	34.3	21.3	.497	.464	3.1	3.7	.513	34.6
9	21.2	.464	.416	2.4	2.3	.471	27.0	20.4	.458	.437	3.2	3.9	.477	36.5	20.9	.471	.453	2.8	2.5	.493	36.9	21.0	.471	.445	2.8	3.3	.488	35.6
10	20.9	.440	.399	2.2	2.5	.448	28.1	20.0	.437	.420	2.6	3.9	.457	37.0	20.5	.454	.433	3.0	2.7	.473	36.4	20.6	.451	.425	2.8	3.3	.467	35.4
11	20.5	.419	.387	2.2	2.3	.429	29.5	19.7	.415	.405	2.5	3.4	.437	38.2	20.2	.425	.412	3.1	3.0	.446	37.7	20.2	.422	.408	2.8	3.1	.442	37.5
12	20.1	.400	.369	2.3	2.5	.410	29.2	19.3	.396	.391	2.6	2.5	.419	39.2	19.9	.406	.392	3.0	3.4	.425	37.3	19.9	.408	.393	2.8	3.5	.426	37.0
13	19.8	.379	.354	2.5	2.5	.389	30.4	19.0	.377	.371	2.7	2.9	.398	38.9	19.5	.379	.373	4.1	4.6	.400	39.0	19.6	.387	.379	2.5	2.9	.408	38.5
14	19.5	.360	.339	2.8	2.7	.371	31.0								19.2	.357	.354	5.0	5.6	.379	39.5	19.2	.366	.363	2.8	3.2	.388	39.4
15	19.1	.338	.324	2.8	2.7	.351	32.5								18.8	.334	.339	5.3	6.6	.358	41.2	18.9	.340	.347	3.1	3.3	.365	41.7
16	18.8	.320	.313	3.0	2.7	.335	34.3																					
17	18.4	.305	.303	2.8	2.5	.322	35.5																					
18	18.1	.287	.292	2.5	2.7	.306	37.3																					

TABLE II. - Continued.

Data point	Run																											
	21							22							23						24							
	Axial position, Z, percent of axial chord from leading edge																											
	50.0							50.0							60.0						60.0							
	Radial position, R, percent of span from hub																											
	50.2							90.3							10.1						50.0							
	Velocity component measurement angles, deg																											
	φ_1 = 20.5 φ_2 = 59.9 N = 1-16							φ_1 = 20.0 φ_2 = 60.2 N = 1-17							φ_1 = 30.1 φ_2 = 69.9 N = 1-15						φ_1 = 30.1 φ_2 = 69.9 N = 1-15							
	Circumferential position, θ, deg	Component critical velocity ratios		Component turbulent intensities, percent		Critical velocity ratio, V/V_{cr}	Flow angle, α, deg	Circumferential position, θ, deg	Component critical velocity ratios		Component turbulent intensities, percent		Critical velocity ratio, V/V_{cr}	Flow angle, α, deg	Circumferential position, θ, deg	Component critical velocity ratios		Component turbulent intensities, percent		Critical velocity ratio, V/V_{cr}	Flow angle, α, deg	Circumferential position, θ, deg	Component critical velocity ratios		Component turbulent intensities, percent		Critical velocity ratio, V/V_{cr}	Flow angle, α, deg
		V_1/V_{cr}	V_2/V_{cr}	σ_1/V	σ_2/V				V_1/V_{cr}	V_2/V_{cr}	σ_1/V	σ_2/V				V_1/V_{cr}	V_2/V_{cr}	σ_1/V	σ_2/V				V_1/V_{cr}	V_2/V_{cr}	σ_1/V	σ_2/V		
1	33.7	.761	.755	4.1	4.7	.805	39.5	24.2	.779	.747	3.1	3.7	.814	36.8	24.5	.718	.703	13.7	15.8	.756	48.3	25.0	.765	.776	9.2	8.4	.820	51.2
2	33.4	.738	.690	4.1	3.9	.762	34.8	23.9	.730	.682	3.7	3.2	.755	34.7	24.1	.768	.757	5.5	5.4	.811	48.8	24.6	.787	.767	3.7	4.2	.827	47.9
3	33.0	.665	.646	3.0	3.4	.697	37.9	23.5	.685	.635	2.8	3.1	.707	34.1	23.8	.750	.722	3.6	4.0	.784	46.9	24.3	.771	.732	3.8	4.1	.802	45.8
4	32.7	.635	.602	2.9	3.7	.659	35.9	23.2	.650	.599	2.7	2.6	.669	33.7	23.4	.725	.685	4.0	3.9	.752	45.6	23.9	.742	.688	3.9	3.9	.764	44.0
5	32.3	.612	.551	2.7	4.9	.624	31.9	22.9	.618	.564	2.6	3.4	.634	33.0	23.1	.695	.647	3.7	3.3	.717	44.3	23.6	.705	.649	3.5	3.5	.725	43.5
6	32.0	.570	.528	3.0	4.3	.587	34.0	22.5	.589	.533	2.8	3.3	.602	32.3	22.8	.674	.621	3.2	2.9	.693	43.5	23.2	.677	.613	3.4	4.9	.692	42.2
7	31.6	.537	.495	3.0	4.3	.552	33.8	22.2	.555	.499	2.9	3.3	.567	31.8	22.4	.639	.598	2.8	2.7	.661	44.7	22.9	.644	.598	4.7	3.0	.664	44.1
8	31.3	.506	.467	3.0	4.0	.520	33.8	21.8	.521	.471	2.8	2.8	.533	32.2	22.1	.614	.572	2.9	3.2	.634	44.3	22.5	.627	.550	2.8	10.5	.636	39.8
9	30.9	.478	.444	3.0	3.4	.492	34.4	21.5	.493	.447	2.9	2.7	.505	32.5	21.7	.590	.543	2.6	3.2	.607	43.5	22.2	.600	.542	2.8	3.7	.613	41.9
10	30.6	.453	.432	3.0	3.5	.471	36.5	21.1	.469	.435	2.7	2.3	.484	34.2	21.4	.562	.517	3.2	3.2	.577	43.4	21.8	.574	.511	2.8	3.7	.584	40.9
11	30.3	.436	.423	2.8	3.1	.457	38.0	20.8	.446	.415	2.4	2.8	.460	34.4	21.0	.540	.488	3.1	3.1	.552	42.2	21.5	.548	.487	2.9	3.2	.558	40.8
12	29.9	.415	.398	2.4	3.4	.433	36.9	20.4	.425	.398	2.7	3.1	.440	35.0	20.7	.508	.465	3.1	2.6	.521	43.0	21.2	.511	.470	3.4	2.8	.525	43.4
13	29.6	.394	.384	2.6	3.4	.414	38.2	20.1	.405	.381	2.6	2.9	.420	35.4	20.3	.482	.450	2.8	2.3	.498	44.5	20.8	.493	.448	2.8	3.0	.505	42.6
14	29.2	.370	.366	2.8	3.6	.391	39.3	19.7	.385	.368	2.6	3.0	.402	36.5	20.0	.463	.437	2.3	2.5	.480	45.4	20.5	.467	.436	3.6	2.6	.483	44.6
15	28.9	.351	.352	2.6	3.2	.373	40.6	19.4	.359	.349	3.3	3.3	.377	37.8	19.6	.443	.418	2.3	3.1	.459	45.5	20.1	.448	.421	4.2	3.4	.464	45.1
16	28.5	.330	.334	2.7	3.5	.353	41.1	19.1	.341	.340	3.3	4.5	.363	39.9														
17								18.7	.319	.329	3.5	3.7	.345	42.5														

TABLE II. - Continued.

Data point	Run																												
	25							26							27						28								
	Axial position, Z, percent of axial chord from leading edge																												
	60.0							60.0							70.0						80.0								
	Radial position, R, percent of span from hub																												
	50.4							90.1							50.0						2.3								
	Velocity component measurement angles, deg																												
	φ_1 = 30.0 φ_2 = 70.0 N = 1-16							φ_1 = 30.1 φ_2 = 69.9 N = 1-15							φ_1 = 35.3 φ_2 = 74.9 N = 1-17						φ_1 = 40.1 φ_2 = 79.8 N = 1-17								
	Circumferential position, θ, deg	Component critical velocity ratios		Component turbulent intensities, percent		Critical velocity ratio, V/V_{cr}	Flow angle, α, deg	Circumferential position, θ, deg	Component critical velocity ratios		Component turbulent intensities, percent		Critical velocity ratio, V/V_{cr}	Flow angle, α, deg	Circumferential position, θ, deg	Component critical velocity ratios		Component turbulent intensities, percent		Critical velocity ratio, V/V_{cr}	Flow angle, α, deg	Circumferential position, θ, deg	Component critical velocity ratios		Component turbulent intensities, percent		Critical velocity ratio, V/V_{cr}	Flow angle, α, deg
		V_1/V_{cr}	V_2/V_{cr}	σ_1/V	σ_2/V				V_1/V_{cr}	V_2/V_{cr}	σ_1/V	σ_2/V				V_1/V_{cr}	V_2/V_{cr}	σ_1/V	σ_2/V				V_1/V_{cr}	V_2/V_{cr}	σ_1/V	σ_2/V		
1	24.9	.780	.782	7.4	7.9	.831	50.2	25.4	.764	.769	11.6	11.1	.815	50.5	26.2	.768	.787	4.3	3.8	.827	57.1	27.4	.701	.736	12.2	12.5	.766	63.9
2	24.5	.790	.766	3.9	4.1	.829	47.6	25.1	.800	.774	4.3	4.2	.838	47.4	25.9	.777	.782	4.1	3.9	.828	55.6	27.0	.739	.764	10.4	11.0	.800	62.6
3	24.2	.761	.727	3.8	3.7	.793	46.3	24.8	.784	.747	3.6	4.5	.816	46.2	25.5	.781	.767	3.3	3.4	.823	53.7	26.7	.773	.785	5.1	4.1	.828	61.2
4	23.9	.737	.687	3.8	4.0	.761	44.5	24.4	.761	.686	4.1	4.9	.777	41.8	25.2	.778	.750	3.2	3.3	.813	52.2	26.3	.778	.773	5.0	6.4	.825	59.5
5	23.5	.704	.648	3.8	4.1	.724	43.6	24.1	.727	.660	4.6	3.6	.744	42.4	24.8	.761	.726	3.0	3.8	.792	51.3	26.0	.775	.758	6.2	7.0	.816	58.3
6	23.1	.670	.615	3.4	3.1	.689	43.2	23.7	.693	.623	3.5	3.3	.708	41.6	24.5	.753	.699	3.6	3.8	.776	49.2	25.6	.737	.748	9.8	7.9	.790	61.2
7	22.8	.647	.594	3.2	2.9	.665	43.4	23.4	.669	.597	3.3	3.1	.682	41.1	24.1	.720	.674	3.6	3.7	.744	49.9	25.3	.767	.747	5.7	5.5	.805	57.9
8	22.5	.621	.563	2.5	4.7	.635	42.4	23.0	.644	.569	3.0	3.5	.654	40.4	23.8	.700	.647	3.5	3.5	.720	48.9	24.9	.770	.725	5.1	5.7	.797	55.2
9	22.2	.589	.534	3.6	3.7	.603	42.4	22.7	.611	.535	2.8	3.5	.620	39.7	23.5	.681	.619	3.3	3.6	.697	47.5	24.6	.761	.715	4.7	4.8	.788	55.1
10	21.8	.562	.501	4.0	3.7	.573	41.0	22.3	.590	.516	2.9	3.4	.598	39.6	23.1	.651	.595	3.4	3.9	.667	48.0	24.3	.746	.689	5.2	4.6	.768	53.7
11	21.4	.539	.479	3.2	3.1	.548	40.8	22.0	.560	.480	3.0	3.1	.565	38.1	22.8	.647	.577	3.2	4.0	.658	46.2	23.9	.728	.653	4.9	4.4	.743	51.4
12	21.1	.516	.462	3.4	2.6	.526	41.4	21.7	.532	.460	3.0	3.1	.538	38.7	22.5	.617	.554	3.3	4.6	.629	46.6	23.6	.702	.637	4.9	4.2	.718	52.2
13	20.7	.479	.441	2.8	2.8	.493	43.4	21.3	.511	.447	2.8	2.5	.518	39.5	22.1	.592	.526	3.4	4.8	.602	45.8	23.2	.675	.621	6.3	4.4	.693	53.5
14	20.4	.460	.428	3.0	3.3	.475	44.4	21.0	.480	.429	2.8	2.5	.489	41.1	21.7	.559	.501	4.2	4.7	.570	46.4	22.9	.644	.609	5.0	3.6	.668	55.5
15	20.1	.443	.415	2.4	4.0	.458	44.9	20.6	.457	.413	2.4	2.4	.468	42.0	21.4	.543	.491	3.9	3.9	.555	47.1	22.5	.639	.603	4.6	4.5	.663	55.4
16	19.7	.422	.395	3.4	4.7	.436	45.0								21.1	.520	.475	3.9	3.2	.533	48.0	22.2	.616	.575	4.6	4.7	.636	54.4
17															20.7	.494	.453	3.7	3.3	.507	48.4	21.8	.610	.558	3.7	6.1	.625	53.1

TABLE II. - Continued.

Data point	Run																													
	29							30							31						32									
	Axial position, Z, percent of axial chord from leading edge																													
	80.0							80.0							80.0						80.0									
	Radial position, R, percent of span from hub																													
	9.9							49.8							49.8						49.8									
	Velocity component measurement angles, deg																													
	φ_1 = 40.0 φ_2 = 80.0 N = 1-16							φ_1 = 40.0 φ_2 = 80.0 N = 1-17							φ_1 = 40.1 φ_2 = 80.0 N = 1-19						φ_1 = 40.2 φ_2 = 79.8 N = 1-18										
	Circumferential position, θ, deg	Component critical velocity ratios		Component turbulent intensities, percent		Critical velocity ratio, V/V_{cr}	Flow angle, α, deg	Circumferential position, θ, deg	Component critical velocity ratios		Component turbulent intensities, percent		Critical velocity ratio, V/V_{cr}	Flow angle, α, deg	Circumferential position, θ, deg	Component critical velocity ratios		Component turbulent intensities, percent		Critical velocity ratio, V/V_{cr}	Flow angle, α, deg	Circumferential position, θ, deg	Component critical velocity ratios		Component turbulent intensities, percent		Critical velocity ratio, V/V_{cr}	Flow angle, α, deg
		V_1/V_{cr}	V_2/V_{cr}	σ_1/V	σ_2/V				V_1/V_{cr}	V_2/V_{cr}	σ_1/V	σ_2/V				V_1/V_{cr}	V_2/V_{cr}	σ_1/V	σ_2/V				V_1/V_{cr}	V_2/V_{cr}	σ_1/V	σ_2/V		
1	27.2	.799	.799	4.5	4.1	.850	60.0	27.6	.773	.781	4.5	3.6	.827	60.8	28.1	.735	.758	10.5	10.2	.795	62.5	27.8	.743	.757	9.0	9.6	.797	61.4
2	26.8	.802	.787	4.2	4.2	.846	58.5	27.2	.774	.774	3.4	3.5	.824	60.0	27.7	.757	.773	7.1	7.0	.814	61.7	27.5	.776	.776	5.9	5.7	.825	60.0
3	26.5	.799	.781	3.5	3.5	.841	58.2	26.9	.776	.760	3.5	3.6	.817	58.4	27.3	.775	.774	4.0	3.7	.824	60.0	27.1	.771	.769	4.1	3.9	.818	59.9
4	26.1	.798	.773	3.9	4.3	.836	57.6	26.5	.768	.752	3.5	3.3	.809	58.4	27.0	.765	.762	3.9	4.2	.812	59.8	26.8	.770	.761	4.4	4.0	.814	59.1
5	25.8	.793	.760	4.4	4.1	.827	56.7	26.2	.765	.743	3.4	3.6	.803	57.7	26.6	.762	.751	4.0	4.0	.805	58.9	26.4	.769	.750	4.4	4.4	.808	58.1
6	25.4	.790	.751	3.4	3.7	.822	56.1	25.8	.768	.722	---	4.1	.796	55.2	26.3	.763	.743	4.3	4.1	.802	58.0	26.1	.770	.736	3.6	4.0	.802	56.4
7	25.1	.781	.738	3.8	4.1	.811	55.6	25.5	.762	.717	3.5	3.8	.790	55.3	25.9	.756	.729	4.0	4.1	.791	57.2	25.7	.764	.727	3.9	4.3	.794	56.1
8	24.7	.774	.722	4.0	4.1	.800	54.6	25.2	.754	.711	3.5	3.7	.782	55.3	25.6	.748	.716	4.2	4.0	.780	56.6	25.4	.760	.715	4.1	4.1	.787	55.2
9	24.4	.766	.708	4.5	4.2	.789	53.9	24.8	.746	.684	3.8	4.1	.766	53.3	25.2	.745	.704	3.9	3.9	.773	55.6	25.0	.750	.702	3.5	4.2	.775	54.7
10	24.0	.755	.695	4.6	3.6	.777	53.6	24.4	.733	.672	4.1	4.4	.753	53.2	24.9	.741	.696	4.3	4.1	.767	55.1	24.7	.742	.686	4.1	4.0	.764	53.8
11	23.7	.741	.681	4.3	3.6	.762	53.4	24.1	.718	.659	4.1	4.2	.738	53.3	24.6	.734	.671	4.1	4.0	.753	52.9	24.4	.727	.656	4.1	3.3	.743	51.8
12	23.4	.724	.661	4.0	3.7	.743	52.9	23.8	.705	.639	4.1	3.2	.721	52.4	24.2	.719	.659	3.9	3.6	.738	53.2	24.0	.723	.654	3.9	0.0	.739	52.1
13	23.0	.704	.638	3.8	3.0	.721	52.3	23.4	.691	.629	3.3	2.8	.708	52.7	23.9	.714	.641	3.9	3.0	.729	51.6	23.7	.701	.632	3.8	3.3	.716	51.8
14	22.7	.682	.627	3.9	2.8	.701	53.4	23.1	.667	.615	3.9	2.7	.686	53.6	23.5	.695	.631	3.5	2.7	.712	52.4	23.3	.677	.616	3.8	3.1	.693	52.6
15	22.3	.666	.610	3.4	2.8	.684	53.1	22.7	.648	.601	3.5	2.7	.668	54.0	23.2	.668	.612	3.4	2.8	.686	53.1	23.0	.656	.596	3.6	3.6	.672	52.4
16	22.0	.645	.599	3.4	3.4	.665	54.2	22.4	.633	.584	2.8	2.8	.651	53.8	22.8	.660	.599	3.3	2.8	.676	52.4	22.6	.637	.581	3.7	3.9	.653	52.6
17								22.0	.612	.565	2.6	3.6	.630	53.9	22.5	.636	.581	2.9	2.9	.652	53.0	22.3	.614	.568	3.9	3.6	.632	53.8
18															22.1	.617	.569	2.6	3.0	.634	53.7	21.9	.596	.540	3.7	4.8	.610	52.2
19															21.8	.598	.552	3.0	3.4	.616	53.7							

Table II. - Continued.

Data point	Run						
	33						
	Axial position, Z, percent of axial chord from leading edge						
	80.0						
	Radial position, R, percent of span from hub						
	89.5						
	Velocity component measurement angles, deg						
	φ_1 = 40.0 φ_2 = 80.0 N = 1-19						
	Circumferential position, θ, deg	Component critical velocity ratios		Component turbulent intensities, percent		Critical velocity ratio, V/V_{cr}	Flow angle, α, deg
		V_1/V_{cr}	V_2/V_{cr}	σ_1/V	σ_2/V		
1	28.1	.747	.754	5.4	5.1	.799	60.8
2	27.8	.756	.751	4.0	4.1	.802	59.5
3	27.4	.753	.745	4.0	3.5	.797	59.1
4	27.1	.750	.734	4.0	4.5	.790	58.3
5	26.7	.754	.734	5.1	4.1	.792	57.9
6	26.4	.755	.714	3.9	4.4	.784	55.6
7	26.1	.774	.715	4.0	4.1	.797	53.8
8	25.7	.749	.688	4.2	4.9	.770	53.4
9	25.4	.737	.674	6.4	3.7	.756	53.1
10	25.0	.735	.656	3.9	5.3	.749	51.1
11	24.7	.752	.654	4.0	4.0	.762	49.2
12	24.3	.715	.635	3.9	3.2	.728	50.8
13	24.0	.702	.622	4.2	3.0	.714	50.6
14	23.6	.686	.611	4.1	2.8	.699	51.0
15	23.3	.669	.597	3.6	2.8	.682	51.2
16	22.9	.641	.583	3.3	3.1	.657	52.6
17	22.6	.629	.569	3.1	3.3	.644	52.2
18	22.2	.607	.550	2.9	4.0	.621	52.3
19	21.9	.590	.534	3.3	3.4	.604	52.3

Data point	Run						
	34						
	Axial position, Z, percent of axial chord from leading edge						
	80.0						
	Radial position, R, percent of span from hub						
	97.3						
	Velocity component measurement angles, deg						
	φ_1 = 40.0 φ_2 = 79.9 N = 1-18						
	Circumferential position, θ, deg	Component critical velocity ratios		Component turbulent intensities, percent		Critical velocity ratio, V/V_{cr}	Flow angle, α, deg
		V_1/V_{cr}	V_2/V_{cr}	σ_1/V	σ_2/V		
1	27.8	.703	.722	10.0	7.1	.759	62.1
2	27.4	.742	.735	5.3	4.5	.785	59.2
3	27.1	.744	.721	5.3	4.3	.780	57.4
4	26.7	.744	.706	5.3	4.4	.773	55.8
5	26.4	.741	.699	4.6	3.6	.769	55.3
6	26.0	.742	.688	4.1	3.5	.765	53.9
7	25.7	.743	.674	3.7	3.5	.760	52.2
8	25.4	.732	.642	3.7	4.0	.743	49.6
9	25.0	.727	.627	3.7	4.3	.735	48.5
10	24.7	.712	.632	3.7	3.5	.724	50.5
11	24.3	.710	.618	4.0	3.4	.719	49.1
12	24.0	.684	.604	3.6	3.3	.695	50.2
13	23.6	.663	.575	3.8	4.2	.671	48.8
14	23.2	.643	.569	3.8	4.5	.654	50.3
15	22.9	.620	.541	3.8	5.6	.628	49.3
16	22.6	.607	.534	3.7	5.1	.616	50.0
17	22.2	.586	.511	3.9	5.3	.594	49.2
18	21.9	.567	.500	3.7	4.8	.576	50.0
19							

Data point	Run						
	35						
	Axial position, Z, percent of axial chord from leading edge						
	90.1						
	Radial position, R, percent of span from hub						
	9.9						
	Velocity component measurement angles, deg						
	φ_1 = 43.1 φ_2 = 83.0 N = 1-18						
	Circumferential position, θ, deg	Component critical velocity ratios		Component turbulent intensities, percent		Critical velocity ratio, V/V_{cr}	Flow angle, α, deg
		V_1/V_{cr}	V_2/V_{cr}	σ_1/V	σ_2/V		
1	29.6	.689	.696	18.3	19.1	.737	63.9
2	29.2	.818	.824	6.9	6.0	.873	63.6
3	28.8	.827	.818	3.9	4.0	.875	62.3
4	28.5	.820	.808	3.7	3.8	.866	61.9
5	28.2	.813	.792	3.6	3.7	.854	61.0
6	27.8	.805	.779	3.3	4.4	.844	60.6
7	27.5	.797	.766	4.0	4.3	.832	60.0
8	27.1	.792	.751	3.9	4.6	.823	58.9
9	26.8	.788	.745	3.9	4.6	.818	58.8
10	26.4	.778	.731	4.2	4.6	.806	58.2
11	26.1	.770	.719	4.0	4.6	.795	57.7
12	25.7	.766	.701	4.2	4.1	.786	56.1
13	25.4	.765	.692	3.9	4.2	.782	55.2
14	25.1	.759	.686	4.5	4.2	.776	55.2
15	24.7	.757	.675	4.0	4.0	.771	54.1
16	24.4	.752	.664	4.3	4.6	.764	53.4
17	24.0	.747	.659	4.9	5.0	.759	53.3
18	23.6	.733	.647	5.2	5.7	.745	53.3
19							

Data point	Run						
	36						
	Axial position, Z, percent of axial chord from leading edge						
	90.1						
	Radial position, R, percent of span from hub						
	50.0						
	Velocity component measurement angles, deg						
	φ_1 = 43.8 φ_2 = 83.0 N = 1-19						
	Circumferential position, θ, deg	Component critical velocity ratios		Component turbulent intensities, percent		Critical velocity ratio, V/V_{cr}	Flow angle, α, deg
		V_1/V_{cr}	V_2/V_{cr}	σ_1/V	σ_2/V		
1	29.7	.806	.816	3.4	3.3	.861	64.4
2	29.3	.803	.812	3.1	---	.858	64.3
3	29.0	.797	.797	2.9	3.0	.846	63.5
4	28.6	.792	.788	2.7	2.7	.839	63.0
5	28.3	.789	.785	2.9	2.8	.835	63.1
6	28.0	.781	.768	2.9	3.0	.822	62.0
7	27.6	.776	.758	3.0	3.3	.815	61.4
8	27.3	.770	.743	3.0	3.2	.804	60.5
9	26.9	.763	.728	3.2	3.5	.793	59.6
10	26.6	.753	.714	3.1	3.5	.780	59.2
11	26.2	.745	.688	3.2	3.9	.765	57.1
12	25.9	.741	.677	3.4	3.7	.759	56.3
13	25.5	.734	.669	3.4	3.3	.751	56.0
14	25.2	.726	.654	3.9	4.2	.740	55.1
15	24.9	.720	.640	4.2	3.8	.732	54.1
16	24.5	.722	.640	3.8	2.8	.733	53.9
17	24.2	.711	.636	4.8	3.5	.724	54.4
18	23.8	.710	.630	4.8	3.7	.721	54.0
19	23.5	.701	.631	5.4	4.1	.715	55.0

TABLE II. - Continued.

Data point	Run																													
	37							38							39							39 continued							
	Axial position, Z, percent of axial chord from leading edge																													
	90.1							100.2							153.2							153.2							
	Radial position, R, percent of span from hub																													
	89.9							50.0							10.1							10.1							
	Velocity component measurement angles, deg																													
	φ_1 = 43.8 φ_2 = 83.0 N = 1-19							φ_1 = 45.1 φ_2 = 85.1 N = 1-21							φ_1 = 45.0 φ_2 = 85.2 N = 1-71							φ_1 = 45.0 φ_2 = 85.2 N = 1-71							
	Circumferential position, θ, deg	Component critical velocity ratios		Component turbulent intensities, percent		Critical velocity ratio, V/V_{cr}	Flow angle, α, deg	Circumferential position, θ, deg	Component critical velocity ratios		Component turbulent intensities, percent		Critical velocity ratio, V/V_{cr}	Flow angle, α, deg	Circumferential position, θ, deg	Component critical velocity ratios		Component turbulent intensities, percent		Critical velocity ratio, V/V_{cr}	Flow angle, α, deg	Circumferential position, θ, deg	Component critical velocity ratios		Component turbulent intensities, percent		Critical velocity ratio, V/V_{cr}	Flow angle, α, deg
		V_1/V_{cr}	V_2/V_{cr}	σ_1/V	σ_2/V				V_1/V_{cr}	V_2/V_{cr}	σ_1/V	σ_2/V				V_1/V_{cr}	V_2/V_{cr}	σ_1/V	σ_2/V				V_1/V_{cr}	V_2/V_{cr}	σ_1/V	σ_2/V		
1	29.5	.773	.771	3.0	3.1	.819	63.2	31.5	.781	.828	4.8	4.1	.859	69.7	34.9	.785	.762	2.7	3.1	.825	62.8	26.3	.785	.767	2.5	2.6	.827	63.3
2	29.1	.770	.759	3.1	3.3	.811	62.2	31.1	.797	.824	4.2	3.7	.863	67.6	34.6	.782	.750	3.3	3.9	.817	61.8	25.9	.782	.765	2.4	2.8	.824	63.4
3	28.8	.766	.744	3.1	3.4	.802	61.2	30.8	.802	.813	3.0	3.0	.859	66.1	34.2	.764	.736	5.1	4.3	.800	62.2	25.6	.781	.762	2.5	3.0	.822	63.3
4	28.4	.757	.735	---	3.3	.793	61.1	30.4	.802	.814	2.9	2.8	.860	66.2	33.9	.753	.707	6.2	5.5	.781	60.2	25.2	.782	.757	2.8	3.0	.820	62.6
5	28.1	.756	.731	3.3	3.4	.790	60.8	30.0	.830	.823	5.5	4.1	.879	64.4	33.5	.737	.694	6.6	5.8	.765	60.5	24.9	.775	.743	3.5	3.9	.810	61.9
6	27.8	.744	.719	3.3	3.5	.777	60.7	29.7	.797	.792	3.1	2.9	.845	64.6	33.2	.730	.673	6.9	5.5	.752	58.7	24.6	.768	.731	4.3	4.4	.800	61.3
7	27.4	.746	.707	3.3	3.4	.773	59.2	29.4	.801	.791	3.1	3.0	.847	64.1	32.9	.700	.651	7.3	5.3	.723	59.5	24.2	.754	.713	5.5	4.8	.784	60.8
8	27.1	.740	.695	3.5	3.5	.764	58.5	29.0	.806	.783	3.1	3.0	.846	62.9	32.5	.692	.661	7.5	7.5	.722	61.5	23.9	.733	.680	6.7	5.1	.756	59.3
9	26.7	.736	.684	3.5	3.2	.758	57.6	28.7	.785	.766	3.2	3.2	.826	63.2	32.2	.736	.657	7.2	7.3	.751	56.3	23.5	.718	.664	6.7	5.1	.740	59.0
10	26.4	.732	.658	3.9	3.0	.746	55.0	28.3	.778	.752	3.4	3.1	.815	62.3	31.8	.769	.683	5.0	8.8	.783	56.0	23.2	.698	.653	6.8	5.2	.722	60.0
11	26.0	.722	.662	3.7	3.2	.740	56.4	28.0	.769	.732	3.1	3.4	.800	61.3	31.5	.781	.766	3.4	4.6	.824	63.6	22.8	.693	.649	6.9	6.1	.718	60.0
12	25.7	.715	.647	3.7	2.8	.730	55.5	27.6	.766	.731	3.6	3.5	.799	61.4	31.1	.786	.777	3.2	3.2	.832	64.2	22.5	.699	.663	7.1	7.6	.727	61.1
13	25.3	.708	.639	3.6	2.7	.722	55.3	27.3	.751	.707	4.1	3.8	.778	60.3	30.8	.789	.779	2.8	3.1	.835	64.1	22.1	.723	.719	6.6	8.1	.768	64.7
14	25.0	.702	.629	3.8	2.6	.715	54.7	26.9	.747	.710	3.5	3.9	.777	61.1	30.4	.794	.781	2.5	2.8	.839	63.8	21.8	.771	.761	3.5	4.0	.816	64.1
15	24.6	.700	.626	3.7	2.4	.712	54.7	26.6	.734	.681	3.5	3.7	.757	59.2	30.1	.792	.784	2.6	2.3	.839	64.3	21.5	.780	.770	2.6	2.9	.825	64.1
16	24.3	.698	.618	3.6	2.4	.708	53.8	26.3	.725	.659	3.6	3.7	.743	57.7	29.7	.792	.783	2.4	2.5	.839	64.2	21.1	.784	.765	2.3	2.4	.826	63.3
17	23.9	.696	.619	3.6	2.5	.708	54.1	25.9	.718	.657	4.1	3.4	.737	58.1	29.4	.794	.783	2.1	2.2	.840	64.1	20.8	.783	.773	2.6	2.4	.829	64.1
18	23.6	.683	.617	4.0	2.3	.697	55.4	25.6	.699	.633	3.5	3.5	.715	57.3	29.1	.793	.782	2.1	2.1	.839	64.1	20.4	.780	.775	2.9	2.5	.828	64.6
19	23.3	.669	.609	3.9	2.8	.684	56.0	25.2	.692	.610	3.6	4.3	.703	55.3	28.7	.790	.780	2.3	2.3	.837	64.1	20.1	.777	.767	2.6	2.6	.823	64.1
20								24.9	.676	.608	4.2	3.4	.690	56.8	28.4	.790	.780	2.1	2.3	.837	64.1	19.7	.784	.776	2.5	2.5	.831	64.3
21								24.5	.678	.603	4.3	3.7	.690	56.0	28.0	.789	.778	2.2	2.6	.835	64.1	19.4	.780	.781	2.5	2.4	.831	65.2
22															27.7	.787	.776	2.2	2.4	.832	64.0	19.0	.769	.776	3.0	2.5	.822	65.8
23															27.3	.779	.776	2.6	2.2	.828	64.8	18.7	.780	.775	2.3	2.7	.828	64.5
24															26.9	.786	.774	2.2	2.2	.831	63.9	18.3	.787	.783	2.7	2.5	.836	64.7
25															26.6	.784	.769	2.4	2.7	.827	63.6	18.0	.775	.775	2.3	2.5	.825	65.1

Table II. - Continued.

Data point	Run																											
	39 concluded							40							40 continued							40 concluded						
	Axial position, Z, percent of axial chord from leading edge																											
	153.2							153.2							153.2							153.2						
	Radial position, R, percent of span from hub																											
	10.1							49.8							49.8							49.8						
	Velocity component measurement angles, deg																											
	φ_1 = 45.0 φ_2 = 85.2 N = 1-71							φ_1 = 45.0 φ_2 = 85.2 N = 1-66							φ_1 = 45.0 φ_2 = 85.2 N = 1-66							φ_1 = 45.0 φ_2 = 85.2 N = 1-66						
	Circumferential position, θ, deg	Component critical velocity ratios		Component turbulent intensities, percent		Critical velocity ratio, V/V_{cr}	Flow angle, α, deg	Circumferential position, θ, deg	Component critical velocity ratios		Component turbulent intensities, percent		Critical velocity ratio, V/V_{cr}	Flow angle, α, deg	Circumferential position, θ, deg	Component critical velocity ratios		Component turbulent intensities, percent		Critical velocity ratio, V/V_{cr}	Flow angle, α, deg	Circumferential position, θ, deg	Component critical velocity ratios		Component turbulent intensities, percent		Critical velocity ratio, V/V_{cr}	Flow angle, α, deg
		V_1/V_{cr}	V_2/V_{cr}	σ_1/V	σ_2/V				V_1/V_{cr}	V_2/V_{cr}	σ_1/V	σ_2/V				V_1/V_{cr}	V_2/V_{cr}	σ_1/V	σ_2/V				V_1/V_{cr}	V_2/V_{cr}	σ_1/V	σ_2/V		
1	17.7	.782	.772	2.6	2.6	.828	64.2	34.9	.691	.705	5.2	4.8	.743	66.7	26.3	.727	.731	3.7	3.5	.777	65.6	17.7	.734	.737	3.1	3.2	.783	65.4
2	17.3	.781	.770	2.4	2.4	.826	63.9	34.6	.685	.702	5.0	5.3	.739	67.0	25.9	.718	.722	4.5	3.9	.767	65.6	17.3	.726	.732	3.6	3.5	.776	65.8
3	17.0	.780	.764	2.9	3.3	.822	63.5	34.2	.691	.710	4.9	5.6	.747	67.2	25.6	.697	.707	5.5	4.3	.748	66.2	16.9	.725	.729	---	3.7	.775	65.5
4	16.6	.781	.765	2.4	2.6	.823	63.5	33.9	.696	.721	4.7	5.4	.755	67.9	25.2	.690	.697	5.1	4.6	.738	65.9	16.6	.725	.726	3.5	3.6	.773	65.3
5	16.3	.779	.761	2.7	2.9	.820	63.3	33.6	.712	.734	4.2	5.0	.770	67.5	24.9	.676	.690	4.9	4.6	.727	66.8	16.3	.718	.720	3.9	4.0	.766	65.4
6	15.9	.777	.758	2.5	3.3	.818	63.1	33.2	.718	.745	3.5	3.3	.780	68.0	24.6	.677	.689	4.7	5.6	.728	66.5	15.9	.708	.713	4.5	4.1	.756	65.7
7	15.6	.778	.758	2.8	2.9	.818	63.1	32.9	.725	.749	3.5	3.1	.786	67.7	24.2	.685	.698	4.9	5.7	.737	66.6	15.6	.700	.697	4.7	4.4	.744	64.8
8	15.2	.777	.750	3.2	3.4	.814	62.3	32.5	.724	.751	3.5	---	.786	68.0	23.9	.694	.716	4.5	5.5	.752	67.6	15.2	.674	.685	5.1	5.1	.724	66.3
9	14.9	.768	.734	3.7	4.3	.801	61.7	32.2	.728	.752	3.1	3.0	.789	67.6	23.5	.707	.732	4.2	4.1	.767	67.7	14.9	.679	.674	5.1	5.1	.720	64.6
10	14.5	.759	.712	4.4	4.8	.787	60.2	31.8	.733	.751	3.5	3.1	.791	67.1	23.2	.711	.736	3.6	3.6	.772	67.8	14.6	.672	.672	4.9	5.6	.715	65.2
11	14.2	.749	.703	5.7	5.1	.776	60.1	31.5	.735	.751	3.2	3.0	.792	66.9	22.9	.716	.742	3.4	3.1	.778	67.9	14.2	.671	.689	5.0	6.0	.725	67.1
12	13.8	.735	.685	6.5	5.4	.760	59.6	31.1	.735	.753	3.0	2.9	.793	67.0	22.5	.722	.740	3.1	3.2	.779	67.0	13.8	.688	.702	4.8	5.9	.741	66.8
13	13.5	.703	.657	7.4	5.6	.727	59.9	30.8	.735	.758	3.1	2.7	.796	67.5	22.1	.723	.739	3.3	3.4	.778	66.8	13.5	.701	.721	4.2	5.5	.758	67.3
14	13.2	.692	.645	7.5	5.2	.716	59.6	30.4	.739	.756	3.2	2.9	.797	66.9	21.8	.728	.747	3.1	2.9	.786	67.1	13.2	.710	.734	3.9	3.7	.770	67.7
15	12.8	.702	.645	7.3	6.1	.722	58.5	30.1	.743	.755	3.0	2.9	.798	66.4	21.5	.728	.749	3.5	2.9	.787	67.4	12.8	.717	.732	3.5	3.5	.772	66.8
16	12.5	.711	.701	7.1	8.9	.752	64.0	29.8	.741	.753	3.4	3.1	.796	66.4	21.1	.731	.744	3.0	3.1	.786	66.5	12.5	.720	.737	3.0	3.0	.777	67.0
17	12.1	.746	.745	5.3	6.0	.794	65.0	29.4	.744	.754	2.8	2.6	.798	66.2	20.8	.733	.751	3.4	3.0	.791	67.0							
18	11.8	.767	.762	3.5	3.7	.814	64.6	29.1	.747	.751	2.7	3.2	.798	65.6	20.4	.735	.742	3.1	2.7	.787	65.9							
19	11.4	.779	.766	3.0	3.0	.823	63.8	28.7	.741	.750	3.2	3.3	.794	66.0	20.1	.733	.744	3.3	2.9	.787	66.3							
20	11.1	.773	.761	2.6	3.0	.818	63.9	28.4	.741	.750	3.4	2.7	.794	66.0	19.7	.737	.744	2.8	2.7	.789	65.9							
21	10.7	.774	.761	3.0	3.3	.818	63.8	28.0	.742	.747	2.9	3.0	.793	65.6	19.4	.734	.732	3.2	6.7	.781	64.9							
22								27.7	.740	.748	3.2	2.8	.793	66.0	19.0	.734	.740	3.1	2.8	.785	65.8							
23								27.3	.744	.742	2.7	3.1	.792	64.9	18.7	.736	.736	3.0	3.0	.784	65.2							
24								26.9	.729	.741	3.4	3.2	.783	66.4	18.3	.735	.736	2.7	3.3	.784	65.3							
25								26.6	.732	.739	3.3	2.8	.784	65.9	18.0	.730	.734	3.6	3.2	.780	65.6							

Table II. - Continued.

Data point	Run																							
	41							41 continued								41 concluded								
	Axial position, Z, percent of axial chord from leading edge																							
	153.2							153.2								153.2								
	Radial position, R, percent of span from hub																							
	80.2							80.2								80.2								
	Velocity component measurement angles, deg																							
	φ_1 = 45.0 φ_2 = 85.2 N = 1-60							φ_1 = 45.0 φ_2 = 85.2 N = 1-60								φ_1 = 45.0 φ_2 = 85.2 N = 1-60								
	Circumferential position, θ, deg	Component critical velocity ratios		Component turbulent intensities, percent		Critical velocity ratio, V/V_{cr}	Flow angle, α, deg	Circumferential position, θ, deg	Component critical velocity ratios		Component turbulent intensities, percent		Critical velocity ratio, V/V_{cr}	Flow angle, α, deg	Circumferential position, θ, deg	Component critical velocity ratios		Component turbulent intensities, percent		Critical velocity ratio, V/V_{cr}	Flow angle, α, deg		
		V_1/V_{cr}	V_2/V_{cr}	σ_1/V	σ_2/V				V_1/V_{cr}	V_2/V_{cr}	σ_1/V	σ_2/V				V_1/V_{cr}	V_2/V_{cr}	σ_1/V	σ_2/V				
1	34.9	.730	.702	3.9	4.0	.764	62.0	26.3	.719	.694	3.6	3.7	.753	62.3	17.7	.709	.689	3.3	3.2	.745	62.9		
2	34.6	.723	.699	3.4	4.0	.758	62.4	25.9	.715	.690	3.6	4.1	.749	62.3	17.3	.712	.685	3.3	3.3	.745	62.1		
3	34.2	.727	.697	3.5	4.0	.760	61.8	25.6	.718	.691	3.7	3.9	.751	62.2	16.9	.712	.686	3.6	3.4	.745	62.3		
4	33.9	.722	.692	4.4	4.3	.754	61.8	25.2	.717	.691	3.7	4.0	.750	62.2	16.6	.710	.692	3.7	3.4	.747	63.1		
5	33.5	.717	.681	5.1	4.7	.746	61.0	24.9	.722	.689	3.5	3.8	.753	61.5	16.3	.712	.686	3.4	3.7	.746	62.2		
6	33.2	.703	.668	6.1	4.9	.732	61.2	24.6	.716	.689	3.7	3.7	.749	62.1	15.9	.712	.685	3.4	3.6	.745	62.2		
7	32.9	.689	.648	7.2	5.3	.715	60.3	24.2	.719	.687	3.8	3.8	.750	61.6	15.6	.709	.686	3.7	3.5	.744	62.5		
8	32.5	.676	.639	6.7	4.9	.703	60.7	23.9	.720	.683	4.3	4.4	.749	61.0	15.2	.722	.684	3.7	3.6	.751	61.0		
9	32.2	.666	.626	6.4	4.6	.691	60.4	23.5	.714	.676	5.0	4.5	.742	60.9	14.9	.714	.686	3.4	3.5	.747	62.1		
10	31.8	.651	.621	5.9	4.7	.679	61.5	23.2	.701	.660	6.0	4.9	.727	60.3	14.5	.710	.695	3.5	3.7	.749	63.4		
11	31.5	.659	.622	6.1	4.7	.684	60.6	22.8	.689	.647	6.9	4.9	.714	60.2									
12	31.1	.669	.661	5.9	7.4	.708	64.2	22.5	.671	.632	6.9	4.9	.696	60.4									
13	30.8	.707	.696	5.5	5.6	.748	63.8	22.1	.664	.622	6.4	4.4	.688	60.0									
14	30.4	.727	.703	3.6	3.9	.762	62.5	21.8	.647	.614	6.0	4.3	.673	61.1									
15	30.1	.737	.710	3.0	3.3	.771	62.2	21.5	.648	.610	5.7	4.8	.672	60.4									
16	29.8	.737	.707	3.1	3.1	.770	61.9	21.1	.654	.648	5.7	7.1	.694	64.4									
17	29.4	.735	.710	3.1	3.5	.770	62.5	20.7	.701	.692	4.5	5.3	.742	64.1									
18	29.1	.731	.707	3.2	3.2	.766	62.4	20.4	.718	.696	3.8	3.6	.753	62.6									
19	28.7	.729	.699	3.3	3.5	.762	61.9	20.1	.721	.694	3.4	3.4	.754	62.1									
20	28.4	.731	.702	3.2	3.6	.765	62.0	19.7	.722	.697	3.1	3.1	.756	62.4									
21	28.0	.729	.702	3.4	3.5	.763	62.1	19.4	.717	.713	---	4.6	.761	64.6									
22	27.7	.723	.699	3.6	3.8	.758	62.5	19.0	.713	.710	3.6	3.7	.758	64.8									
23	27.3	.723	.706	3.6	4.5	.761	63.2	18.7	.722	.697	3.4	3.6	.756	62.4									
24	27.0	.720	.692	3.6	4.0	.753	62.1	18.3	.715	.709	3.3	4.0	.759	64.4									
25	26.6	.713	.699	4.0	3.9	.752	63.5	18.0	.719	.684	3.5	3.3	.749	61.3									

Table II. - Concluded.

Data point	Run									
	42					43				
	Axial position, Z, percent of chord from leading edge									
	20.0					50.0				
	Radial position, R, percent of span from hub									
	90.1					50.2				
	Circumferential position, θ, deg									
	19.0					22.3				
	Velocity component measurement angle, φ_j, deg	Component critical velocity ratio, V_j/V_{cr}	Component turbulent intensity, σ_j/V, percent	Critical velocity ratio, V/V_{cr}	Flow angle, α, deg	Velocity component measurement angle, φ_j, deg	Component critical velocity ratio, V_j/V_{cr}	Component turbulent intensity, σ_j/V, percent	Critical velocity ratio, V/V_{cr}	Flow angle, α, deg
1	80.0	.161	3.3	.309	21.8	94.6	.302	3.1	.607	33.9
2	70.0	.208	3.1			79.0	.423	4.6		
3	60.0	.243	3.2			63.5	.531	4.6		
4	50.1	.272	2.9			47.9	.584	4.5		
5	40.0	.294	2.9			32.7	.612	3.4		
6	30.1	.305	2.9			16.9	.581	2.9		
7	20.1	.309	2.9			1.5	.510	2.7		
8	10.0	.301	2.9			-14.0	.408	2.2		
9	- .2	.288	2.8			-29.5	.273	2.6		
10	-10.2	.263	2.7							
11	-20.1	.231	2.9							
12	-30.1	.191	3.3							
13	-30.1	.193	3.2							
14	-40.2	.143	3.2							

TABLE III. - SUMMARY OF EXPERIMENTAL TEST CONDITIONS AND MEASURED SURFACE VANE LOCATIONS

Run	Data point	Survey location		Laser conditions			Cascade conditions				
		Axial position, Z, percent of axial chord	Radial position, R, percent of span	Laser signal filter settings, MHz		Was evaporation condensation used?	Cascade setting pressure, p_h/p_0	Inlet pressure ratio, δ	Inlet critical velocity ratio squared, θ_{cr}	Vane circumferential location, deg	
				Lower	Upper					Suction, θ_s	Pressure, θ_p
1	1-23	1.3	50.2	2	16	No	0.651	0.970	1.066	----	----
2	1-8	10.2	9.9	4	↓	Yes	.650	.974	1.054	22.2	----
2	9-17	-----	----	2		---	-----	-----	-----	----	----
3	1-15	10.2	50.2	4		Yes	.651	.974	1.055	22.9	----
3	16-14	-----	----	2		---	-----	-----	-----	----	----
4	1-11	10.2	90.1	4		Yes	.651	.972	1.058	23.7	----
4	12-22	-----	----	2	↓	---	-----	-----	-----	----	----
5	1-5	20.0	2.3	8	32	Yes	.651	.983	1.040	22.1	----
5	6-18	-----	----	4	16	---	-----	-----	-----	----	----
6	1-5	20.0	9.7	8	32	Yes	.651	.983	1.039	22.2	----
6	6-16	-----	----	4	16	---	-----	-----	-----	----	----
7	1-16	20.0	9.9	4	32	No	.651	.978	1.057	22.3	----
8	1-7	20.0	49.4	8	32	Yes	.651	.983	1.040	22.8	----
8	8-19	-----	----	4	16	---	-----	-----	-----	----	----
9	1-18	20.0	49.8	4	32	Yes	.651	.979	1.054	22.9	----
10	1-6	20.0	90.1	8	32	Yes	.651	.983	1.037	23.6	----
10	7-20	-----	----	4	16	---	-----	-----	-----	----	----
11	1-7	20.0	90.1	8	32	Yes	.651	.985	1.031	23.6	----
11	8-19	-----	----	4	16	---	-----	-----	-----	----	----
12	1-7	20.0	97.4	8	32	Yes	.651	.985	1.030	----	----
12	8-17	-----	----	4	16	---	-----	-----	-----	----	----
13	1-17	30.0	50.2	↓	32	No	.651	.977	1.052	23.1	----
14	1-14	40.1	9.9		32	Yes	↓	.980	1.051	22.8	----
15	1-16	40.1	49.8		↓	Yes		.980	1.053	23.5	----
16	1-16	40.0	50.2			No		.978	1.052	23.5	----
17	1-18	40.1	90.1			Yes		.979	1.049	24.1	----
18	1-13	50.0	10.3			Yes		.972	1.061	23.7	----
19	1-15	↓	50.0			Yes	↓	.972	1.060	24.3	----
20	1-15		50.2			No	.650	.977	1.052	24.3	18.0
21	1-16		50.2			No	.651	.978	1.052	34.2	----
22	1-17		90.3	↓		Yes	↓	.972	1.062	24.8	----
23	1-15	60.0	10.1	8		↓		.976	1.046	24.9	----
24	1-15	↓	50.0	8				.976	1.046	25.5	----
25	1-16		50.4	8				.974	1.052	25.4	----
26	1-15		90.1	4		↓	.652	.976	1.046	25.9	----
27	1-17	70.0	50.0	8		No	.650	.977	1.052	26.9	----
28	1-17	80.0	2.3	↓		No	.651	.971	1.067	28.1	----
29	1-16	↓	9.9			Yes	↓	.977	1.058	28.2	----
30	1-17		49.8			Yes		.978	1.058	28.6	----
31	1-19		49.8			Yes		.980	1.054	28.6	----
32	1-18		49.8			No		.972	1.067	28.5	----
33	1-19		89.5			Yes		.977	1.058	28.8	----
34	1-19	↓	97.3			No	.652	.970	1.067	----	----
35	1-18	90.2	9.9	↓		Yes	.652	.976	1.047	30.5	----
36	1-19	90.2	50.0	16		Yes	.651	.976	1.046	30.7	----
37	1-19	90.2	89.9	16		Yes	.650	.978	1.045	30.9	----
38	1-21	100.2	50.0	8		No	.651	.970	1.067	----	----
39	1-71	153.2	10.1	↓		↓	↓	.976	1.061	----	----
40	1-66	153.2	49.8					.976	1.060	----	----
41	1-60	153.2	80.2	↓	↓	↓		.976	1.058	----	----
42	1-14	20.0	90.1	2	16	Yes		.984	1.030	----	----
43	1-9	50.0	50.2	4	32	No	↓	.978	1.053	----	----

TABLE IV. - INLET BOUNDARY

LAYER PROFILES ONE AXIAL

CHORD UPSTREAM OF VANES

[V_{fs}/V_{cr} = 0.23.]

Distance from wall, y/h, percent	Hub velocity ratio, V_h/V_{fs}	Tip velocity ratio, V_t/V_{fs}
1.00	0.897	0.853
1.25	.942	-----
1.50	.982	.879
1.75	.992	-----
2.00	1.00	.918
3.00	-----	.950
4.00	-----	.967
5.00	-----	.979
6.00	-----	.980
7.00	-----	.987

TABLE V. - VANE SURFACE STATIC PRESSURE MEASUREMENTS AT DESIGN CONDITIONS

(a) Radial position, R, 13.3 percent of span

Axial position, Z, percent of chord	Suction-surface pressure ratio, p_s/p_0'	Pressure-surface pressure ratio, p_p/p_0'
0	0.996	-----
13.3	.837	-----
29.8	.762	-----
31.5	-----	0.963
46.2	.673	-----
66.0	.645	-----
66.8	-----	.877
79.7	.625	-----
84.8	-----	.761
86.4	.606	-----
92.6	.623	-----

(b) Radial position, R, 50 percent of span

Axial position, Z, percent of chord	Suction-surface pressure ratio, p_s/p_0'	Pressure-surface pressure ratio, p_p/p_0'
0.7	0.989	-----
4.0	.896	-----
4.1	-----	0.975
10.0	.812	-----
16.5	-----	.972
19.8	.780	-----
29.8	.720	-----
31.5	-----	.964
39.8	.655	-----
48.9	-----	.939
52.9	.611	-----
66.0	.654	-----
66.6	-----	.881
73.0	.658	-----
75.8	-----	.829
79.7	.640	-----
84.7	-----	.773
86.4	.624	-----
92.5	.637	-----
99.5	.716	-----

(c) Radial position, R, 86.7 percent of span

Axial position, Z, percent of chord	Suction-surface pressure ratio, p_s/p_0'	Pressure-surface pressure ratio, p_p/p_0'
0	0.997	-----
13.3	.786	-----
29.8	.682	-----
31.5	-----	0.960
46.2	.608	-----
66.0	.656	-----
66.8	-----	.878
79.7	.653	-----
84.8	-----	.767
86.4	.647	-----
92.6	.660	----

TABLE VI. - AFTERMIXED FLOW CONDITIONS AND VANE LOSSES FROM PRESSURE PROBE MEASUREMENTS TAKEN 1/3 AXIAL CHORD DOWNSTREAM OF VANE

Radial position, R, percent of span	Flow angle, α_M, deg	Static pressure ratio, p_M/p'_0	Kinetic energy loss coefficient, $\bar{e}_M$	Total pressure loss coefficient, $\frac{p'_0 - p'_M}{p'_0}$
1.1	----	-----	0.269	0.116
2.0	----	-----	.127	.057
3.0	----	-----	.074	.033
4.0	----	-----	.059	.026
5.0	----	-----	.054	.024
6.0	----	-----	.053	.024
7.4	63.6	0.659	.053	.023
10.0	63.4	.661	.063	.027
15.0	64.4	.664	.053	.023
20.0	65.6	.666	.029	.012
25.1	66.5	.669	.027	.011
30.1	66.9	.673	.026	.011
35.0	67.2	.677	.025	.010
40.1	67.6	.680	.022	.009
45.1	67.7	.683	.022	.009
50.0	67.7	.687	.022	.009
55.1	67.6	.689	.022	.009
60.1	67.2	.693	.022	.008
65.1	67.0	.697	.025	.009
70.1	66.1	.701	.040	.014
75.1	65.1	.706	.053	.019
80.1	64.7	.709	.054	.019
85.1	65.2	.713	.043	.015
90.2	67.1	.716	.037	.013
94.9	72.1	.722	.058	.019
96.2	----	-----	.067	.022
97.2	----	-----	.084	.028
98.2	----	-----	.139	.045
99.1	----	-----	.296	.093

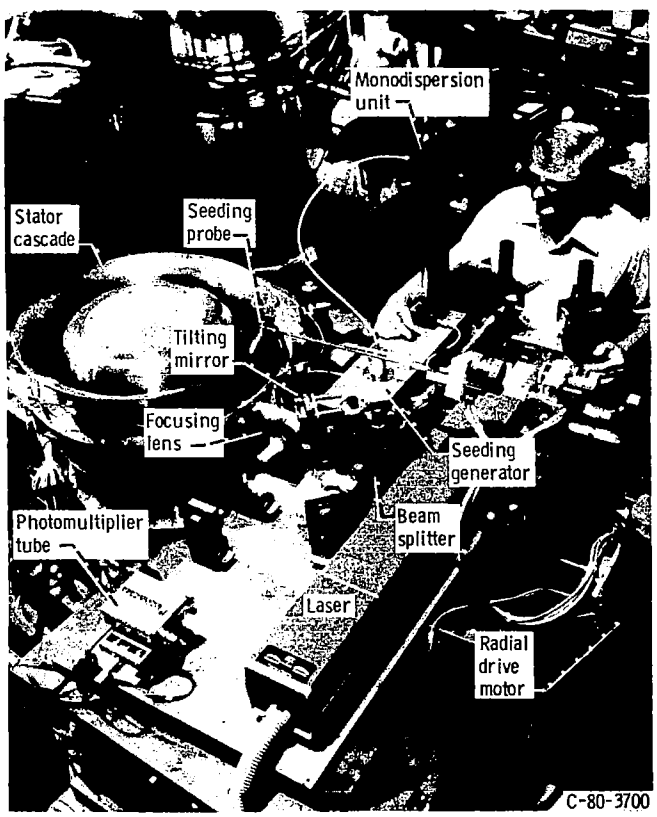

Figure 1. - Core stator annular cascade and laser anemometer.

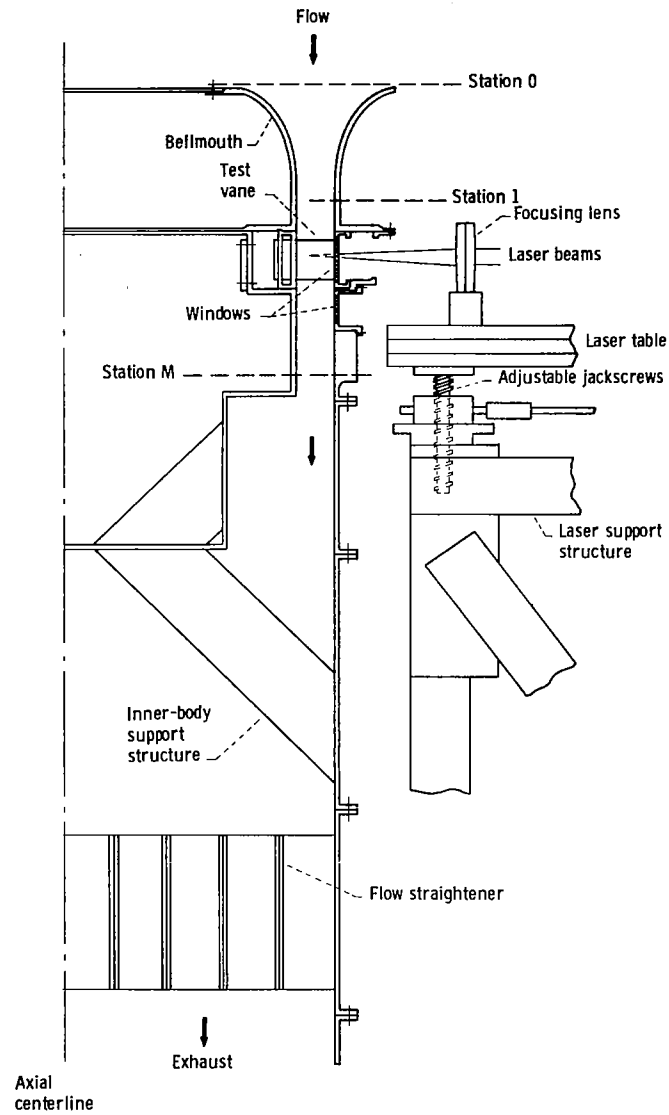

Figure 2. - Schematic cross-sectional view of core turbine stator cascade.

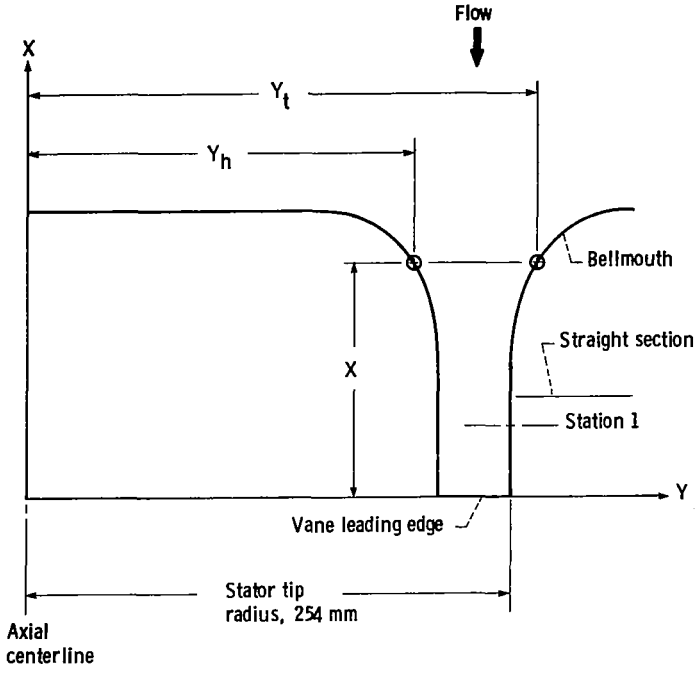

X	Y_t	Y_h
0	1.000	0.850
.209	1.000	.850
.274	1.001	.849
.301	1.002	.848
.340	1.005	.845
.369	1.008	.842
.393	1.013	.837
.415	1.018	.832
.434	1.024	.826
.451	1.030	.820
.467	1.036	.814
.481	1.043	.807
.507	1.058	.792
.529	1.074	.776
.547	1.091	.759
.564	1.109	.742
.582	1.136	.714
.596	1.165	.686
.602	1.184	.666
.606	1.203	.647
.609	1.231	.619
.610	—	0

(All values nondimensionalized by stator tip radius, 254 mm)

Figure 3. - Annular cascade inlet bellmouth geometry.

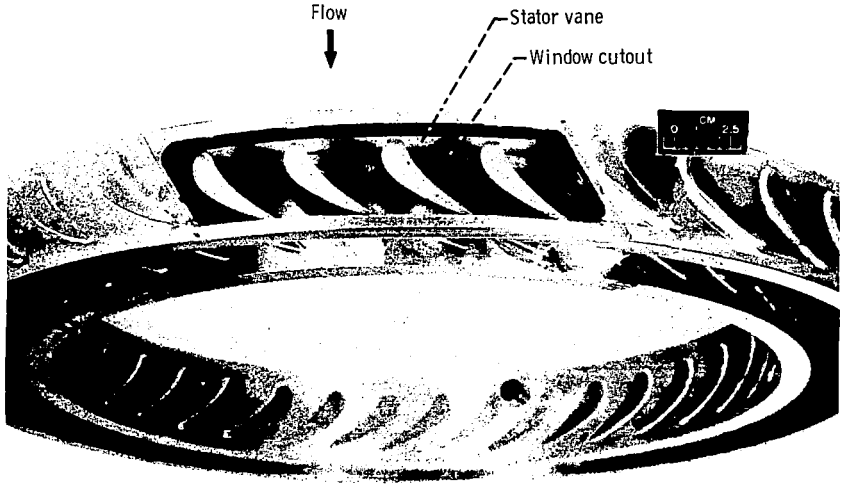

Figure 4. - Stator vane ring showing cutout for laser window.

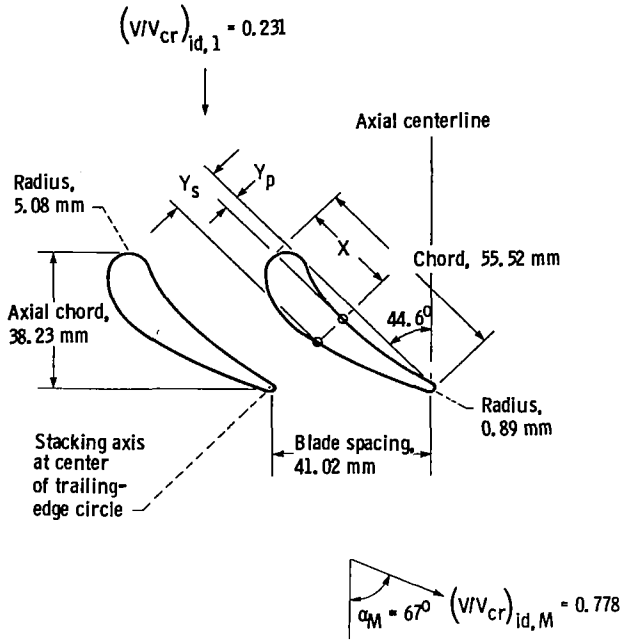

X	Y_p	Y_s
0	0.091	0.091
.023	—	.153
.046	—	.181
.069	—	.202
.091	—	.218
.114	—	.231
.137	.011	.242
.160	.021	.250
.183	.029	.257
.206	.036	.261
.229	.043	.263
.252	.048	.265
.274	.053	.266
.320	.059	.263
.366	.065	.257
.412	.068	.248
.457	.069	.238
.503	.069	.226
.549	.066	.215
.595	.064	.200
.640	.059	.185
.686	.054	.170
.732	.047	.153
.778	.040	.134
.823	.032	.114
.869	.023	.094
.915	.015	.072
.961	.005	.048
1.000	.016	.016

(All values nondimensionalized by chord, 55.52 mm)

Figure 5. - Core turbine stator vane geometry at mean section.

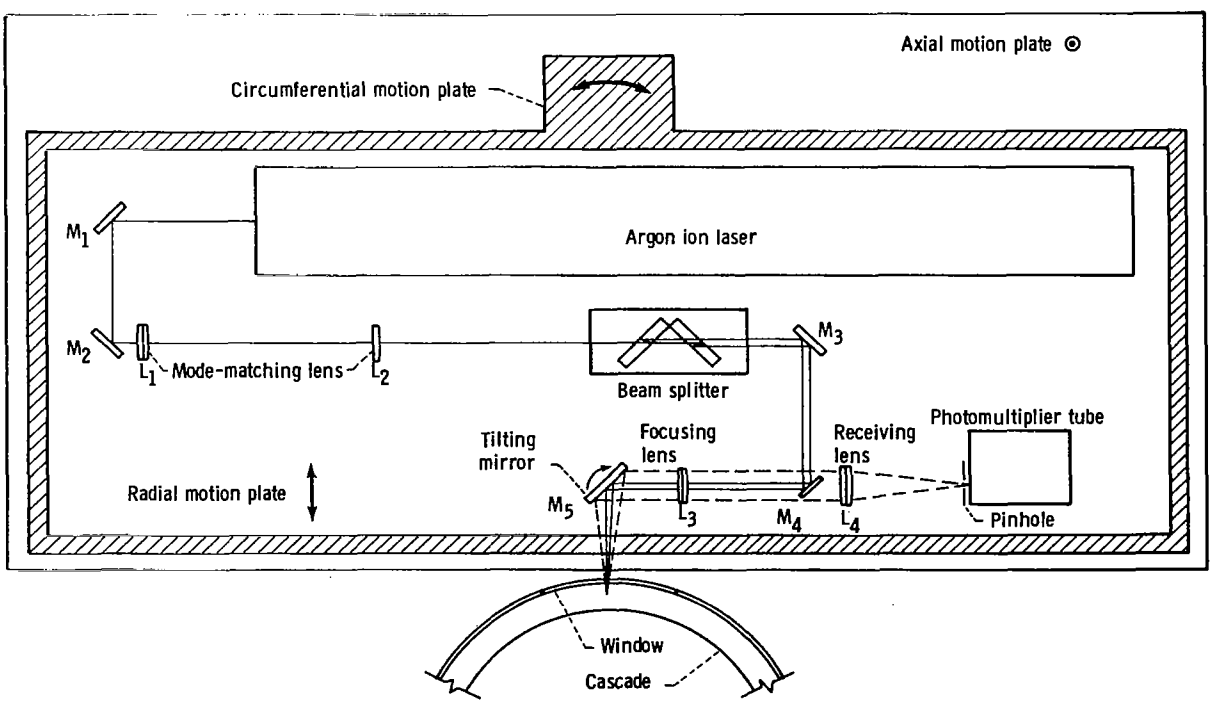

Figure 6. - Schematic of laser anemometer and transversing mechanism.

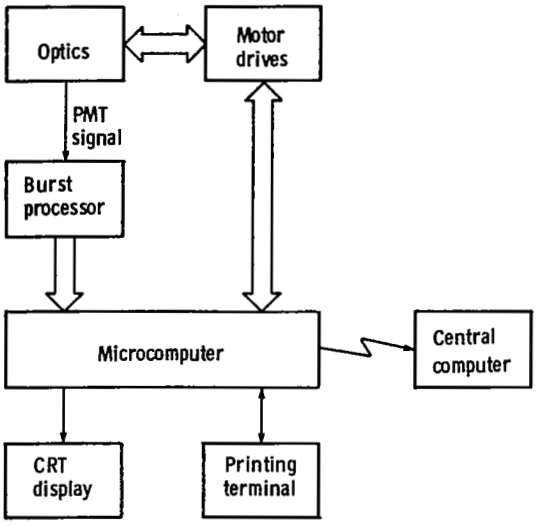

Figure 7. - Block diagram of laser anemometer system.

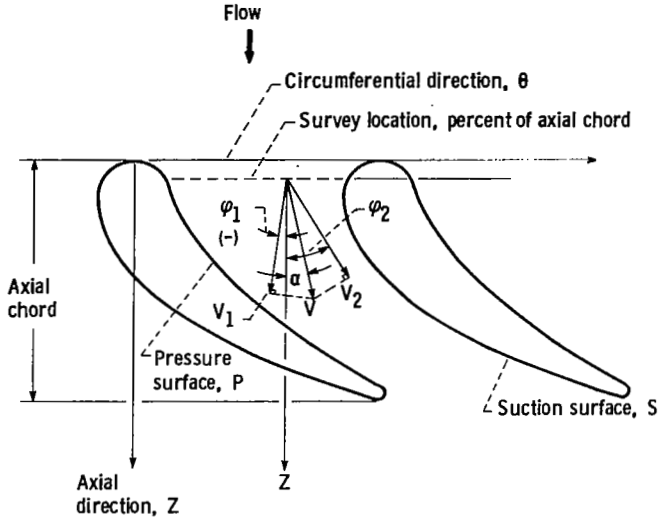

Figure 9. - Nomenclature and orientation of velocity component measurements for laser anemometer surveys.

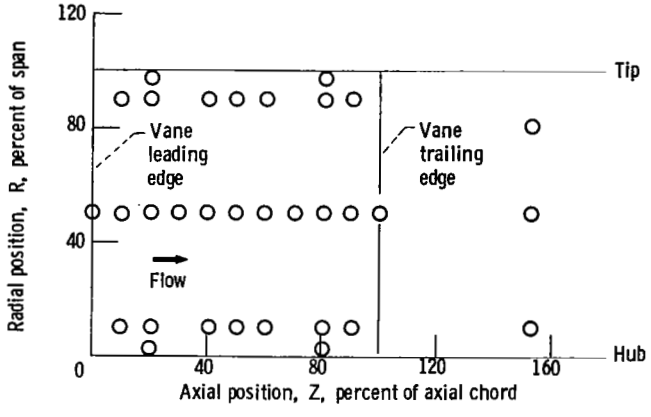

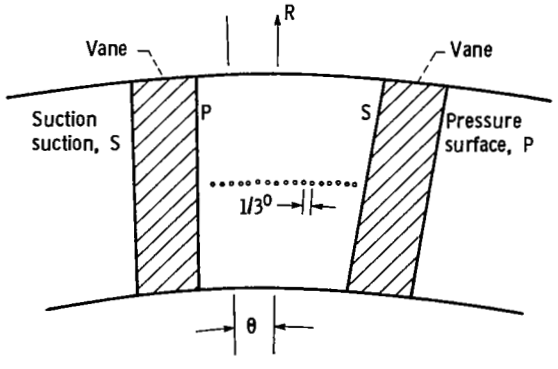

Figure 8. - Laser survey measurement locations.

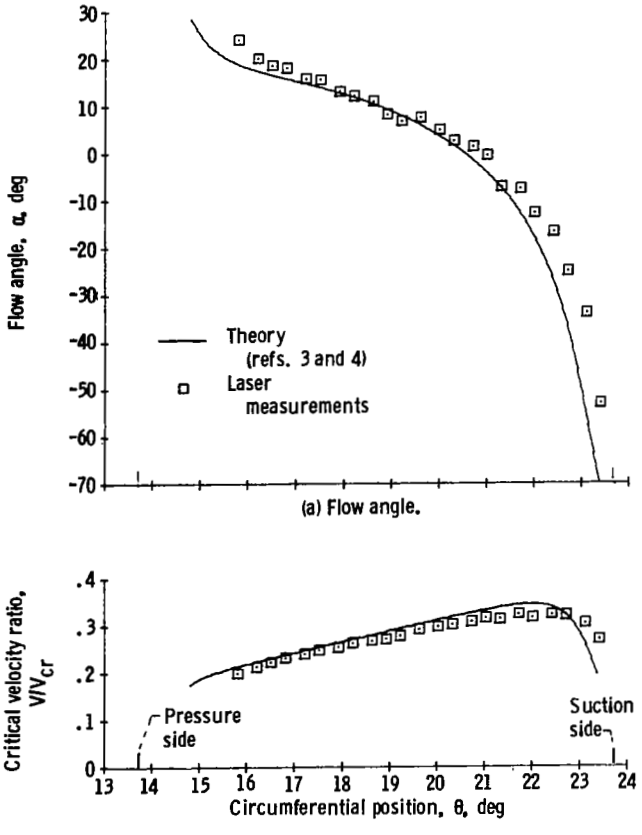

Figure 10. - Comparison of laser measurements with theory at 1.3 percent of axial chord. Radial position, R, 50.2 percent of span.

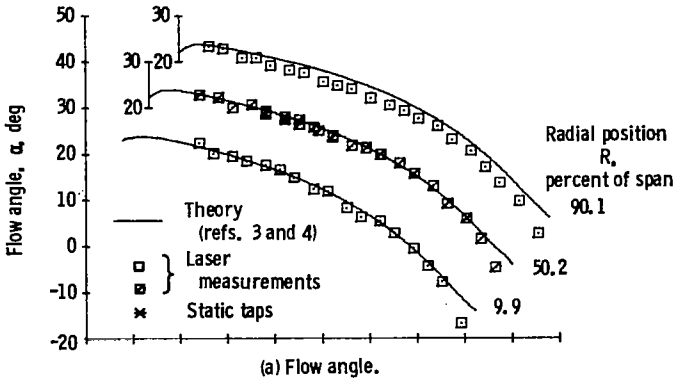

(a) Flow angle.

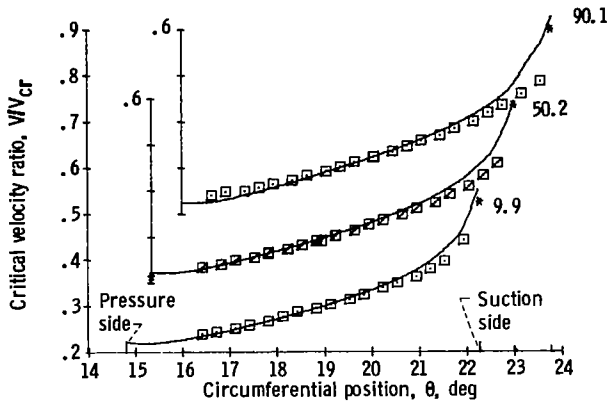

(b) Critical velocity ratio.

Figure 11. - Comparison of laser measurements with theory at 10.2 percent of axial chord.

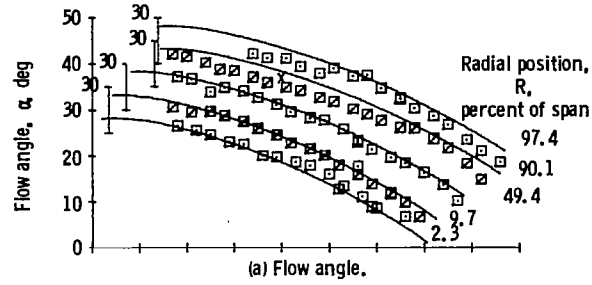

(a) Flow angle.

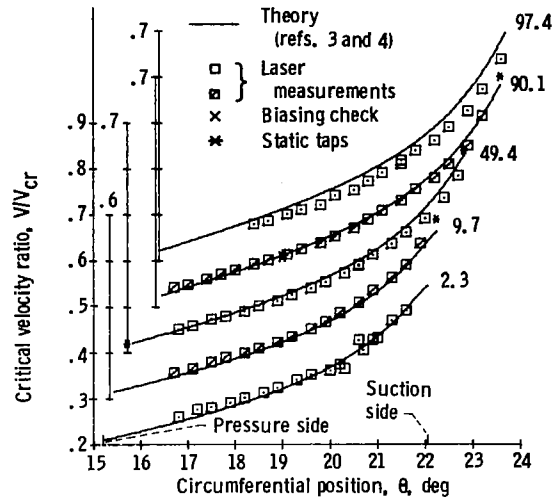

(b) Critical velocity ratio.

Figure 12. - Comparison of laser measurements with theory at 20.0 percent of axial chord.

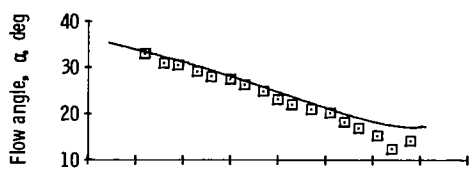

(a) Flow angle.

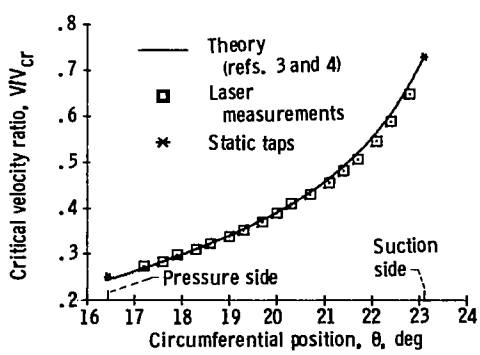

(b) Critical velocity ratio.

Figure 13. - Comparison of laser measurements with theory at 30.0 percent of axial chord. Radial position, R, 50.2 percent of span.

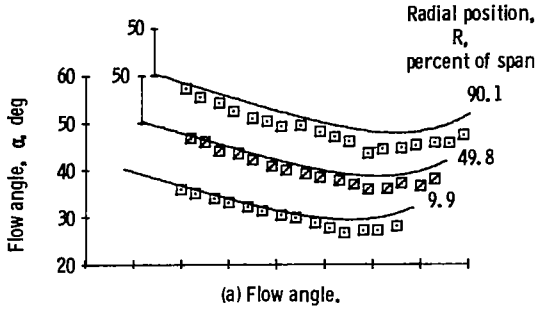

(a) Flow angle.

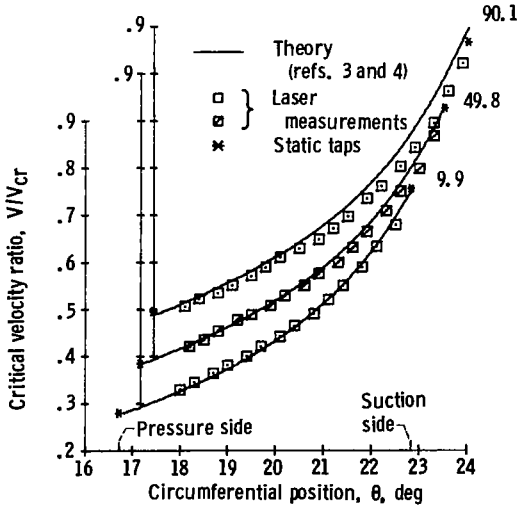

(b) Critical velocity ratio.

Figure 14. - Comparison of laser measurements with theory at 40.1 percent of axial chord.

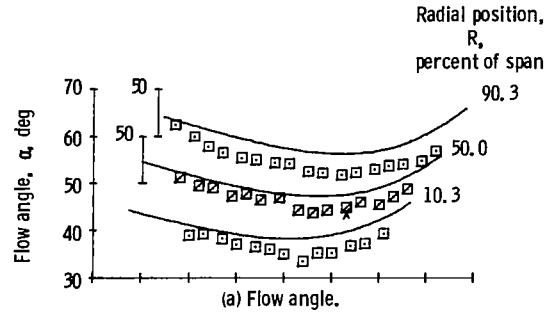

(a) Flow angle.

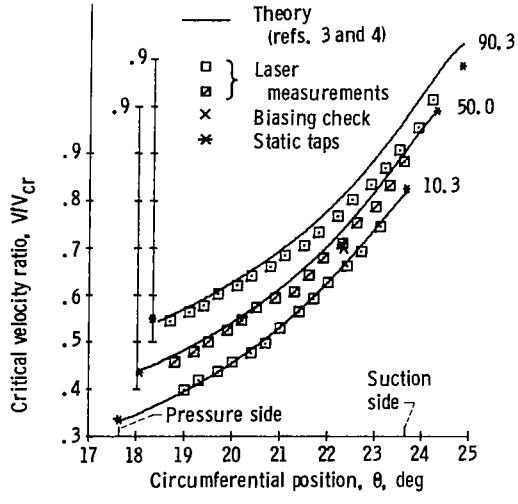

(b) Critical velocity ratio.

Figure 15. - Comparison of laser measurements with theory at 50.0 percent of axial chord.

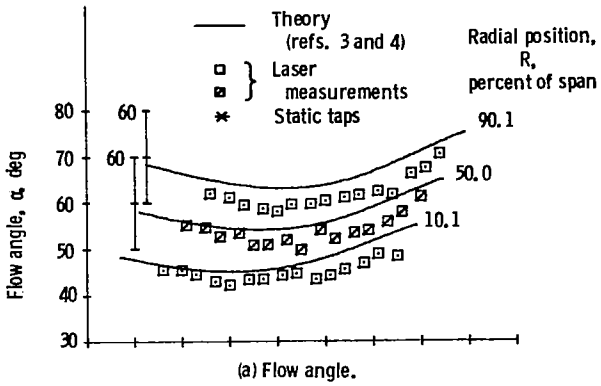

(a) Flow angle.

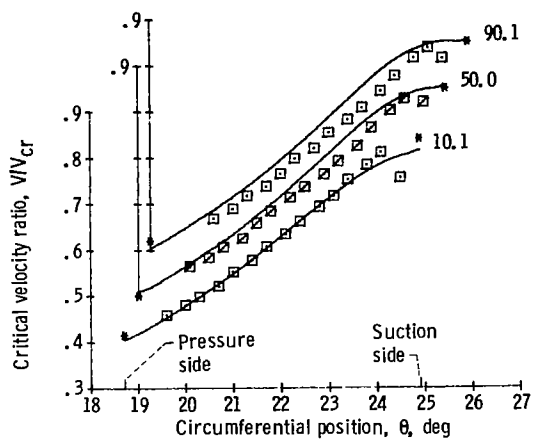

(b) Critical velocity ratio.

Figure 16. - Comparison of laser measurements with theory at 60.0 percent of axial chord.

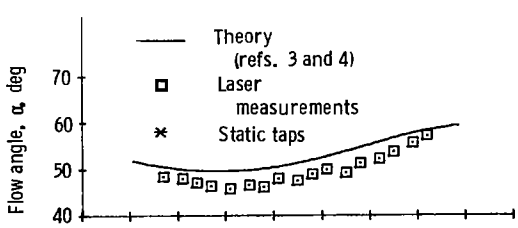

(a) Flow angle.

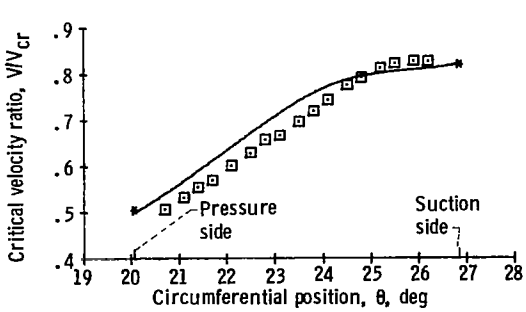

(b) Critical velocity ratio.

Figure 17. - Comparison of laser measurements with theory at 70.0 percent of axial chord. Radial position, R, 50.0 percent of span.

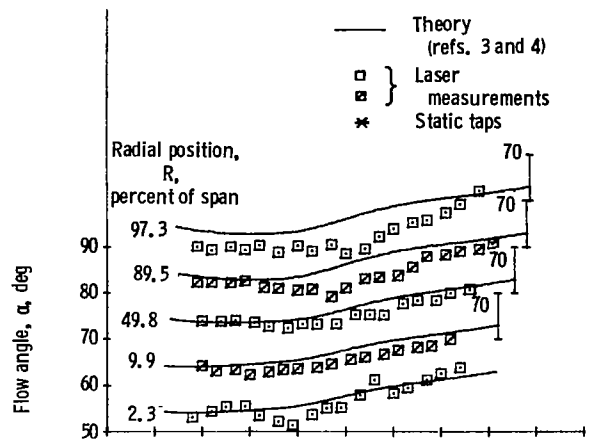

(a) Flow angle.

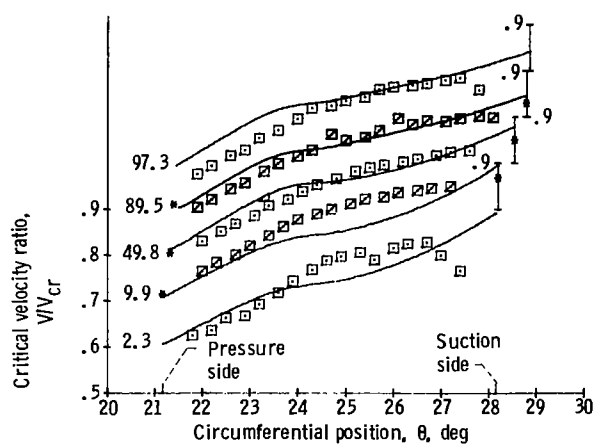

(b) Critical velocity ratio.

Figure 18. - Comparison of laser measurements with theory at 80.0 percent of axial chord.

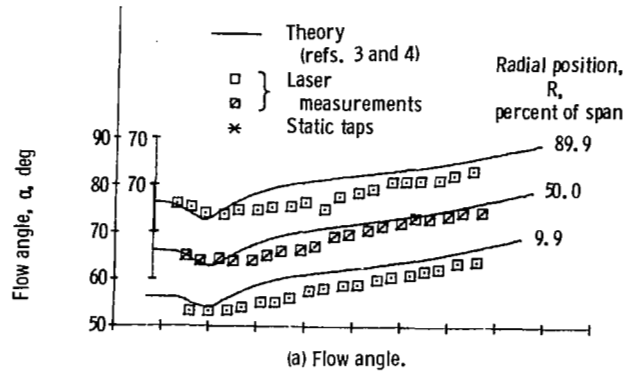

(a) Flow angle.

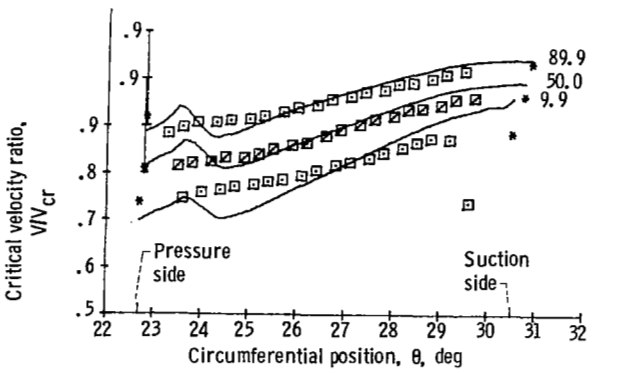

(b) Critical velocity ratio.

Figure 19. - Comparison of laser measurements with theory at 90.1 percent of axial chord.

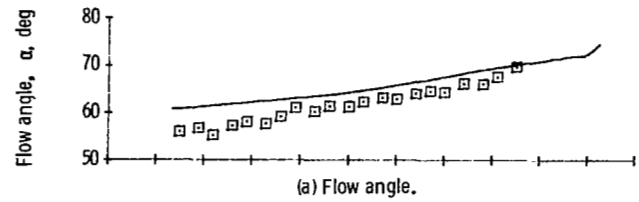

(a) Flow angle.

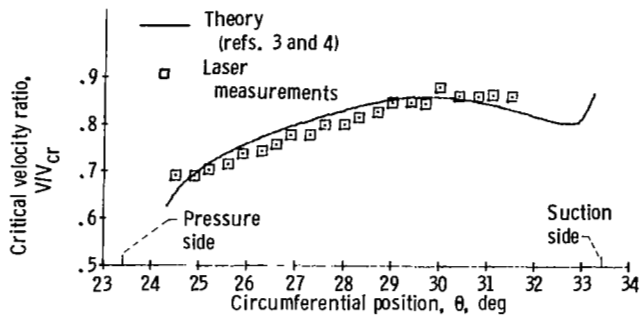

(b) Critical velocity ratio.

Figure 20. - Comparison of laser measurements with theory at 100.2 percent of axial chord. Radial position, R, 50.0 percent of span.

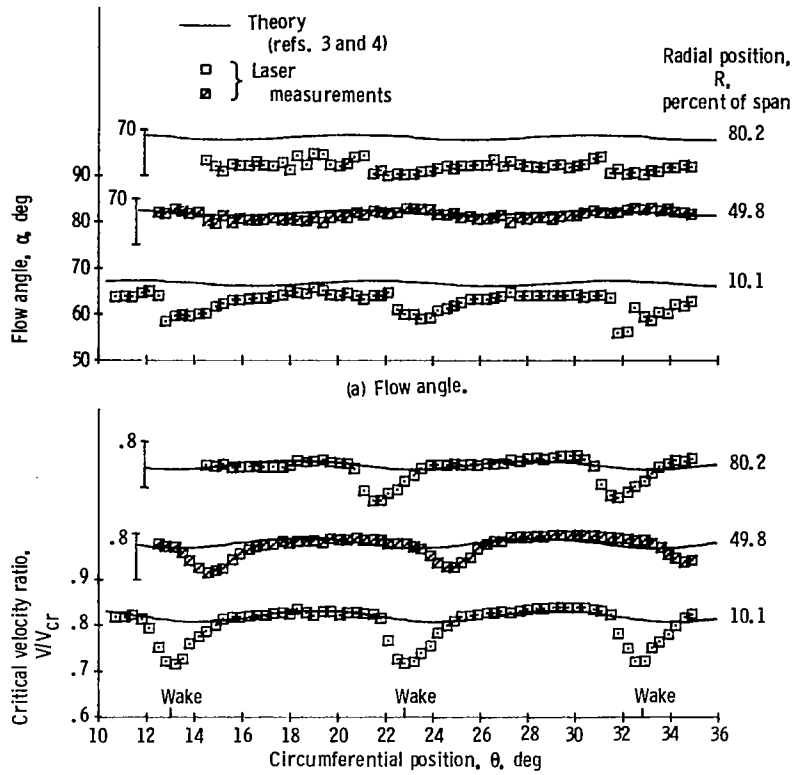

Figure 21. - Comparison of laser measurements with theory at 153.2 percent of axial chord.

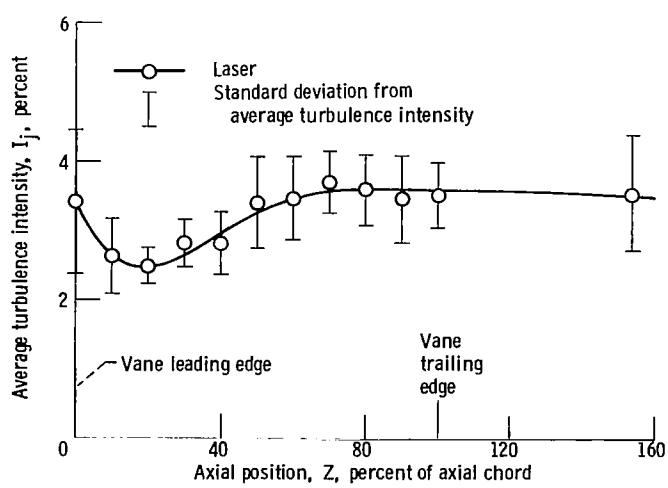

Figure 22. - Circumferential average turbulence intensity as a function of axial position in cascade at mean radius.

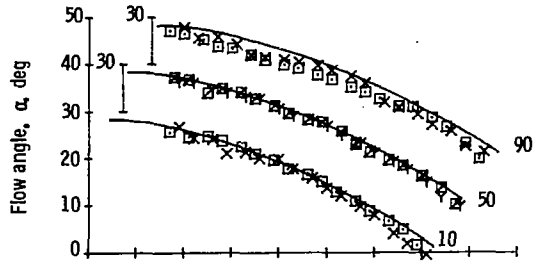

(a) Flow angle.

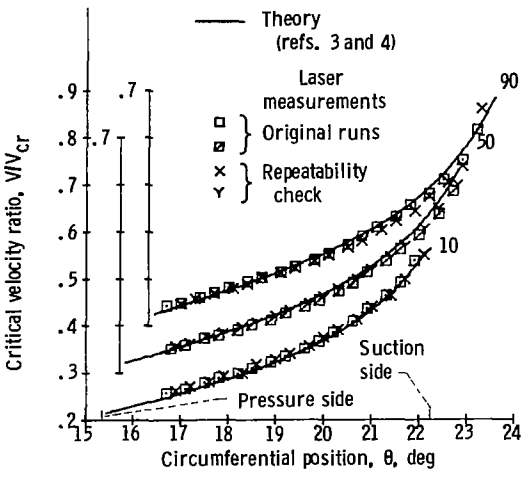

(b) Critical velocity ratio.

Figure 23. - Repeatability of laser measurements at 20.0 percent of axial chord.

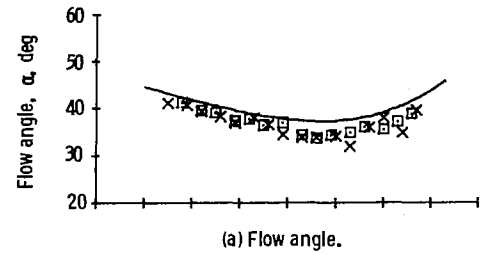

(a) Flow angle.

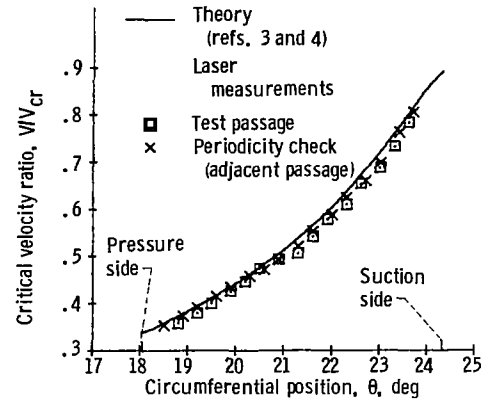

(b) Critical velocity ratio.

Figure 24. - Periodicity of laser measurements at 50.0 percent of axial chord. Radial position, R, 50.0 percent of span.

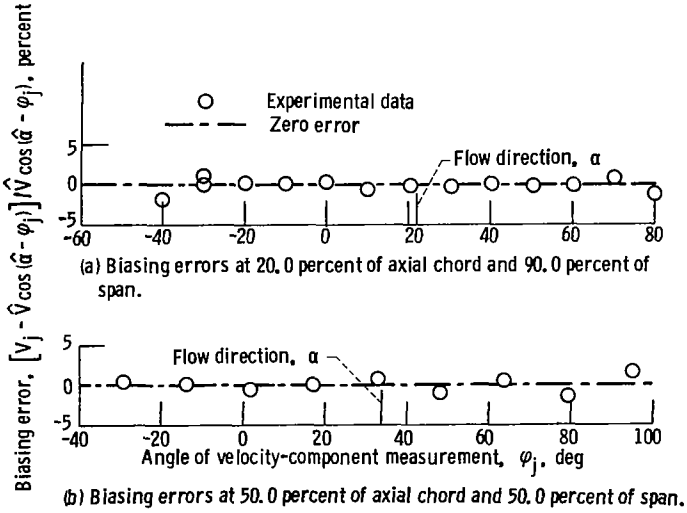

(a) Biasing errors at 20.0 percent of axial chord and 90.0 percent of span.

(b) Biasing errors at 50.0 percent of axial chord and 50.0 percent of span.

Figure 25. - Biasing of velocity-component measurements within vane passage.

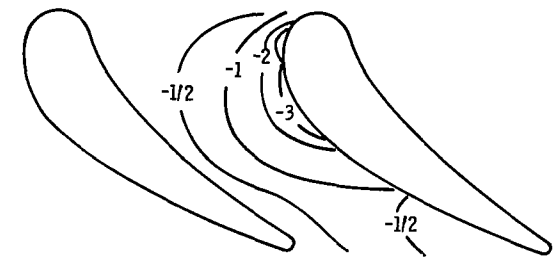

(a) Flow angle difference, $\alpha_P - \alpha_G$, deg.

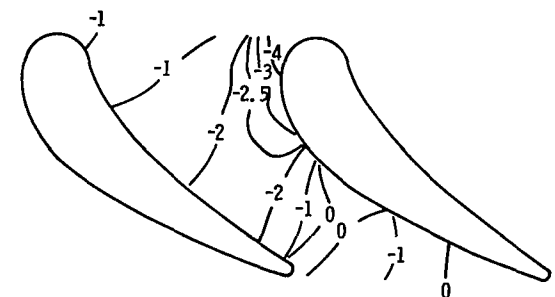

(b) Velocity difference, $(V_P - V_G)/V_G$, percent.

Figure 26. - Mean-radius dynamic behavior of 1.2-μm-diameter particles entrained in airflow.

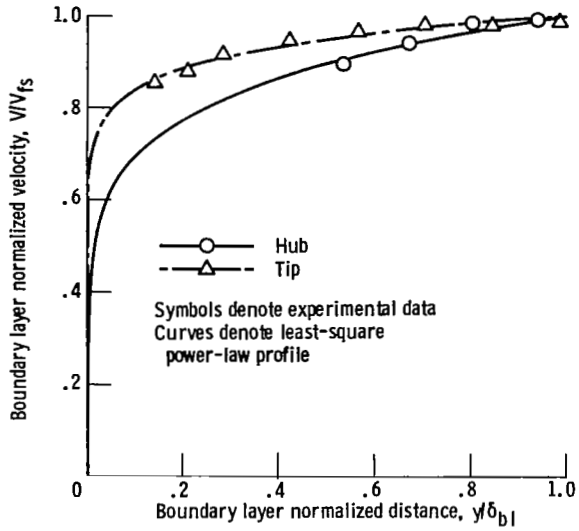

Figure 27. - Endwall boundary layer profiles one axial chord upstream of stator vanes.

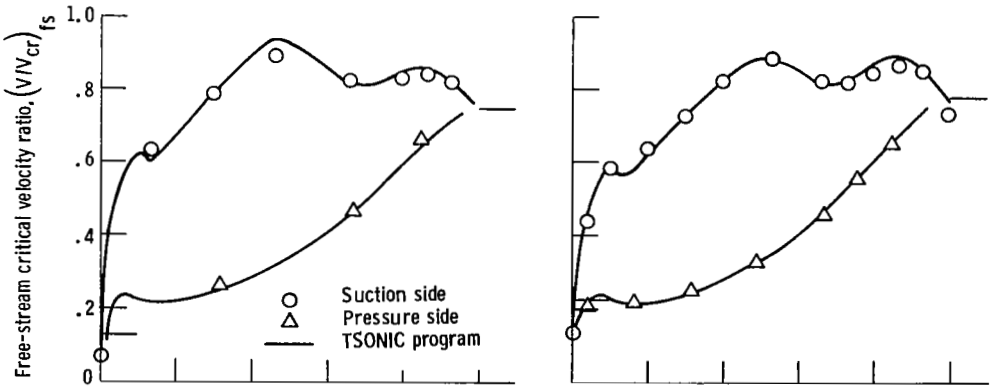

(a) Radial position, R, 86.7 percent of span from hub.

(b) Radial position, R, 50.0 percent of span from hub.

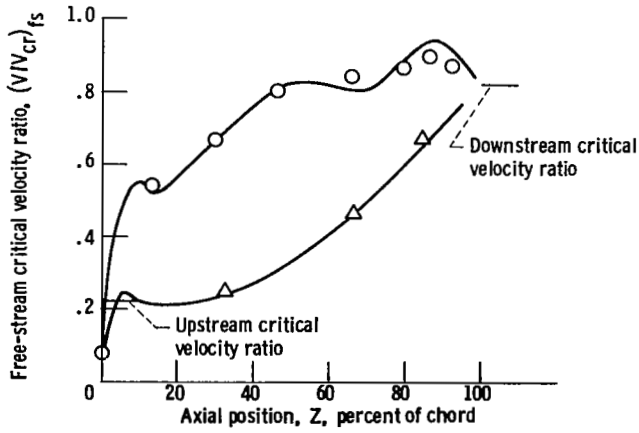

(c) Radial position, R, 13.3 percent of span from hub.

Figure 28. - Distribution of free-stream critical velocity ratio around vane at design conditions (velocities calculated from surface static pressure measurements).

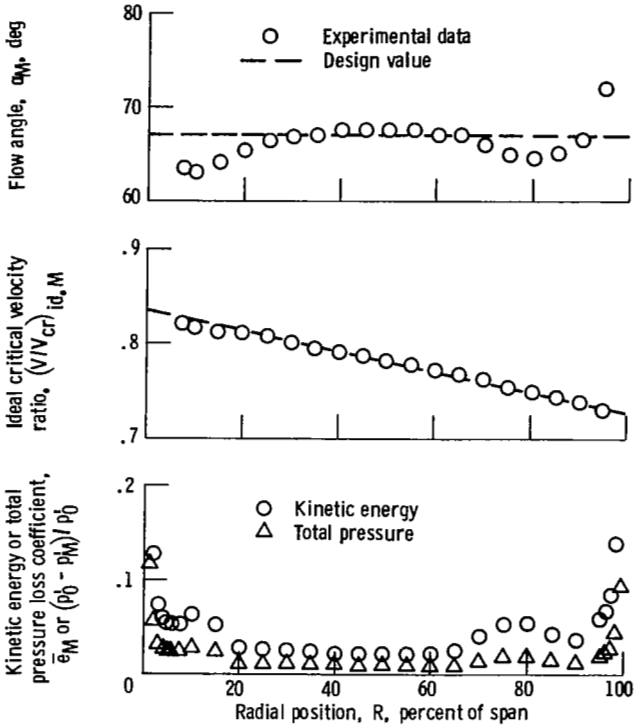

Figure 29. - Aftermixed flow conditions and vane losses from pressure probe measurements taken 1/3 axial chord downstream of vanes.

1. Report No.	2. Government Accession No.	3. Recipient's Catalog No.
NASA TP-2018		

4. Title and Subtitle	5. Report Date
LASER ANEMOMETER MEASUREMENTS IN AN ANNULAR CASCADE OF CORE TURBINE VANES AND COMPARISON WITH THEORY	June 1982
	6. Performing Organization Code 505-32-2B
7. Author(s)	8. Performing Organization Report No.
Louis J. Goldman and Richard G. Seasholtz	E-876
	10. Work Unit No.
9. Performing Organization Name and Address	
National Aeronautics and Space Administration Lewis Research Center Cleveland, Ohio 44135	11. Contract or Grant No.
	13. Type of Report and Period Covered
12. Sponsoring Agency Name and Address	Technical Paper
National Aeronautics and Space Administration Washington, D. C. 20546	14. Sponsoring Agency Code

15. Supplementary Notes

16. Abstract

Laser measurements were made in an annular cascade of stator vanes operating at an exit critical velocity ratio of 0.78. Velocity and flow angles in the blade-to-blade plane were obtained at every 10 percent of axial chord within the passage and at 1/2 axial chord downstream of the vanes for radial positions near the hub, mean, and tip. Results are presented in both plot and tabulated form and are compared with calculations from an inviscid, quasi-three-dimensional computer program. The experimental measurements generally agreed well with these theoretical calculations, an indication of the usefulness of this analytic approach.

17. Key Words (Suggested by Author(s))
Velocity measurements
Laser anemometer
Stator intervane flow field
Experimental and analytical comparison

18. Distribution Statement
Unclassified - unlimited
STAR Category 02

19. Security Classif. (of this report)	20. Security Classif. (of this page)	21. No. of Pages	22. Price*
Unclassified	Unclassified	46	A03

* For sale by the National Technical Information Service, Springfield, Virginia 22161

NASA-Langley, 1982

National Aeronautics and
Space Administration

Washington, D.C.
20546

Official Business
Penalty for Private Use, $300

THIRD-CLASS BULK RATE

Postage and Fees Paid
National Aeronautics and
Space Administration
NASA-451

U.S.MAIL

S

NASA

POSTMASTER: If Undeliverable (Section 158
Postal Manual) Do Not Return